



Syntectonic magmatism and reactivation of collisional structures during late-Variscan shearing (SW Sardinia, Italy)

F. Secchi¹ · L. Casini¹ · F. Cifelli² · S. Naitza³ · E. Carta¹ · G. Oggiano¹

Received: 28 June 2021 / Accepted: 8 April 2022
© The Author(s) 2022

Abstract

The Arbus igneous complex (SW Sardinia, Italy) represents a good example of a short time lived post-collisional composite pluton emplaced at shallow crustal level in the external zone of the Variscan chain. The pluton almost consists of granodiorite and leucogranite rock-suites emplaced at 304 ± 1 Ma within a main NW trending thrust separating the metamorphic wedge from the fold and thrust belt foreland. The pluton emplaced into a dilatational step over connecting two NW–SE dextral shear zones which belongs to a regional network of post-collisional strike-slip structures marking the transition from collision to post-collisional extension. The microstructure observed for quartz and K-feldspar confirms the lack of significant post-emplacment deformation, indicating only limited high-temperature sub-solidus recrystallization. Anisotropy of magnetic susceptibility data and field-structural analysis have been carried out to reconstruct the geometry of the pluton and the trajectories of magmatic flow in relation to regional deformation structures. Overall, the magmatic and the magnetic fabrics are broadly discordant with the metamorphic foliation of the country rocks, defining an EW trending elliptical asymmetric sill rooted in the SW quadrant. The reconstructed architecture combined to petrologic observation indicates that accretion of the pluton involved injection of multiple dykes through a sub-vertical feeder zone, combined to lateral flow of the roof controlled by inherited collisional structure. The duration of magmatic activity and the cooling history of the contact metamorphic aureole have been evaluated through a suite of 2D thermal models. All these observations, together with the available geochronological constraints are suggestive of very rapid construction of the pluton. The proposed emplacement model is fully consistent with the regional phase of strike-slip tectonics and widespread magmatism accommodating the large rotation of the Corsica-Sardinia block during the Carboniferous-Permian transition.

Keywords Pluton cooling · Pluton emplacement · AMS data · Thermal model

Introduction

The anisotropy of magnetic susceptibility (AMS) is widely used to constrain the deformation history of magmatic rocks (King 1966; Van der Voo and Klootwijk 1972; Heller 1973; Ellwood and Whitney 1980; Guillet et al. 1983; Cogné and Perroud 1988; Bouchez et al. 1990; Mamtani and Greiling 2005; Cifelli et al. 2012), particularly wherever macroscopic

flow markers are poorly developed as commonly observed for rocks of broadly granitic composition (Bouchez 1997; Aranguren et al. 2003; Kratinova et al. 2003; Sant’Ovaia et al. 2010; Brown 2013).

Despite the widespread acceptance of AMS as an effective tool for the analysis of magmatic systems, only a few data are available for the Sardinia-Corsica Batholith (Gattaceca et al. 2004; Edel et al. 2014). The complex structure of this late-Variscan batholith resulted from coalescence of several magmatic events (Rossi and Cocherie 1991; Cocherie et al. 2005), clustered in Sardinia in two main peaks (Casini et al. 2015a; Cuccuru et al. 2016). The first phase of magmatic activity around 320–315 Ma is mostly coincident with regional strike-slip deformation accommodated by NW–SE and E–W crustal-scale shear zones (Casini et al. 2012; 2015a,b). Remarkably, the onset of second phase (~300 Ma; Cuccuru et al. 2016; Naitza et al. 2017; Conte et al. 2017)

✉ F. Cifelli
francesca.cifelli@uniroma3.it

¹ Dipartimento di Scienze Chimiche, Fisiche, Matematiche e Naturali, Università Degli Studi di Sassari, Sassari, Italy

² Dipartimento di Scienze, Università Degli Studi Roma Tre, Roma, Italy

³ Dipartimento Scienze Chimiche e Geologiche. Università Degli Studi di Cagliari, Cagliari, Italy

is synchronous with the Late Variscan drifting and overall $> 90^\circ$ clockwise rotation recorded by the Corsica-Sardinia block (Edel et al. 2014). A pervasive network of roughly EW and NW trending strike-slip shear zones, often reactivating collisional structures, testifies this regional phase of shearing (Conti et al. 1998, 2001; Casini et al. 2010; Cuccuru et al., 2012; Casini and Funedda 2014). Although a few works have documented the connection between shear zones and Late Variscan magmatism, the significance of this geodynamic event remains still enigmatic (Gébelin et al. 2009; Casini et al. 2012; 2015a; Musumeci et al. 2015).

This paper focuses on the emplacement of the Arbus pluton, a composite late Carboniferous (304 ± 1 Ma) pluton exposed in southwestern Sardinia (Italy) for which a complete set of geological and petrological data are available (Secchi et al. 1991; Cuccuru et al. 2016). The pluton records incremental accretion by injection of several magma pulses within a huge transtensional EW shear zone (Capo Pecora Shear Zone, Fig. 1b), that reactivates the frontal thrust of the Variscan metamorphic wedge during post-collisional shearing (Casini et al. 2015a). A field structural mapping combined with microstructural analysis and AMS data are used to refine the shape and internal fabric of the pluton, as well as the surrounding contact metamorphic aureole. The overall structural constraints complement the existing geochronological and petrologic dataset, providing new insights into the mechanisms of magmatic accretion in relation to late Variscan tectonics. The applicability of different rapid to slow incremental growth histories characterized by variable melt injection rate and frequency of the magmatic injections are then evaluated by forward 2D numerical modelling, using a purely thermal version of the finite difference code *evp2d* (Casini 2012; Casini et al. 2013; Casini and Maino 2018). The simulated thermal histories are used to pinpoint the rates and persistence of late Variscan magmatism in relation to regional tectonics. Finally, the results obtained in this work are recast in the general framework of the south Variscan chain and discussed in terms of post-collisional geodynamic evolution of the orogen.

Geological setting and petrographical features

The Arbus pluton forms a roughly elliptical EW trending pluton injected within the Arburese Frontal Thrust (AFT), a major W-directed collisional structure that separates the greenschist metamorphic wedge from the Variscan Foreland (Fig. 1a, b) (Funedda 2009). The pluton is made of a felsic core composed of cordierite-bearing leucogranites, rimmed by three pyroxene-, hornblende- and biotite-bearing granodioritic shells (Fig. 1c). A small diaper of monzo-gabbronorite composition (MG) exposed along the northern contact of the

pluton represents the most mafic endmember (Fig. 1c). U/Pb geochronological constraints on zircons from pyroxene-bearing granodiorites (GD1) indicate that the pluton emplaced at about 304 ± 1 Ma (Cuccuru et al. 2016) matching the onset of a large $> 90^\circ$ clockwise rotation of the Sardinia-Corsica block (Edel et al. 2014) connected to late orogenic shearing of the Variscides (Matte 2001; Gutiérrez-Alonso et al. 2009; Casini and Funedda 2014; Musumeci et al. 2015).

The small scatter of U/Pb zircon ages recorded by GD1 samples (Cuccuru et al. 2016) indicates that the whole magmatic system likely solidified in less than 1 Ma, as commonly observed in upper-crustal plutons of similar size and emplacement depth (i.e., Barboni and Schoene 2014). This observation is fully consistent with the prevalence of fine- to medium-grained rock-types, the ductile and gradational contacts between different magma batches, the shallow emplacement depth < 0.2 GPa (Bosi et al. 2018) and the narrow contact aureole dominated by andalusite-cordierite spotted schists (Fig. 1c). Similarly to all the intrusions observed in SW Sardinia, the Arbus pluton shows distinctive compositional and mineralogical characters of a typical ilmenite rock-series. The pluton is a sill-like body (Fig. 2a) showing normal zoning with the mafic magma batches (orthopyroxene—and hornblende-bearing granodiorite, monzo-gabbronorite Fig. 2b, e) in the external part of the complex and progressively more differentiated products (cordierite-bearing leucogranite) in the core (Fig. 1c). In addition, LG1 leucogranites at the core of intrusion are coarse-grained rocks. A detailed full petrographic characterization can be found in Secchi et al. (1991) and Secchi and D'Antonio (1996) and is summarized in Table 1.

Hypidiomorphic rock-textures are by far dominant; porphyritic varieties are only recorded for quartz monzo-gabbronorites which show in addition graphic textures of groundmasses. Evidence for deformation is suggested by chessboard appearance of interstitial quartz (Fig. 3), locally observed only in granitic rocks and their rare monzonitic dark enclaves.

A typical petrographic feature of Arbus igneous rocks is the occurrence of orthopyroxene + clinopyroxene + red dark mica well distinguishable from gabbroic rocks to GD1 granodiorites. In addition, a rather diffuse wide-spread sub-solidus alteration, producing cumingtonite and actinolitic hornblende as uralitic phases on original orthopyroxene and clinopyroxene, respectively, is commonly observed in GD1 granodiorites. Conversely, in hornblende-bearing granodiorites (GD2) and biotite-bearing granodiorites (GD3), pyroxenes are only observed as drop-like inclusions of plagioclase and euhedral hornblende or red biotite represent the only mafic phases. In GD3 and LG rocks, dark mica show a siderophyllitic composition (replaced by white mica) and unusually extremely Fe-rich cordierite of sekaninitic composition (replaced

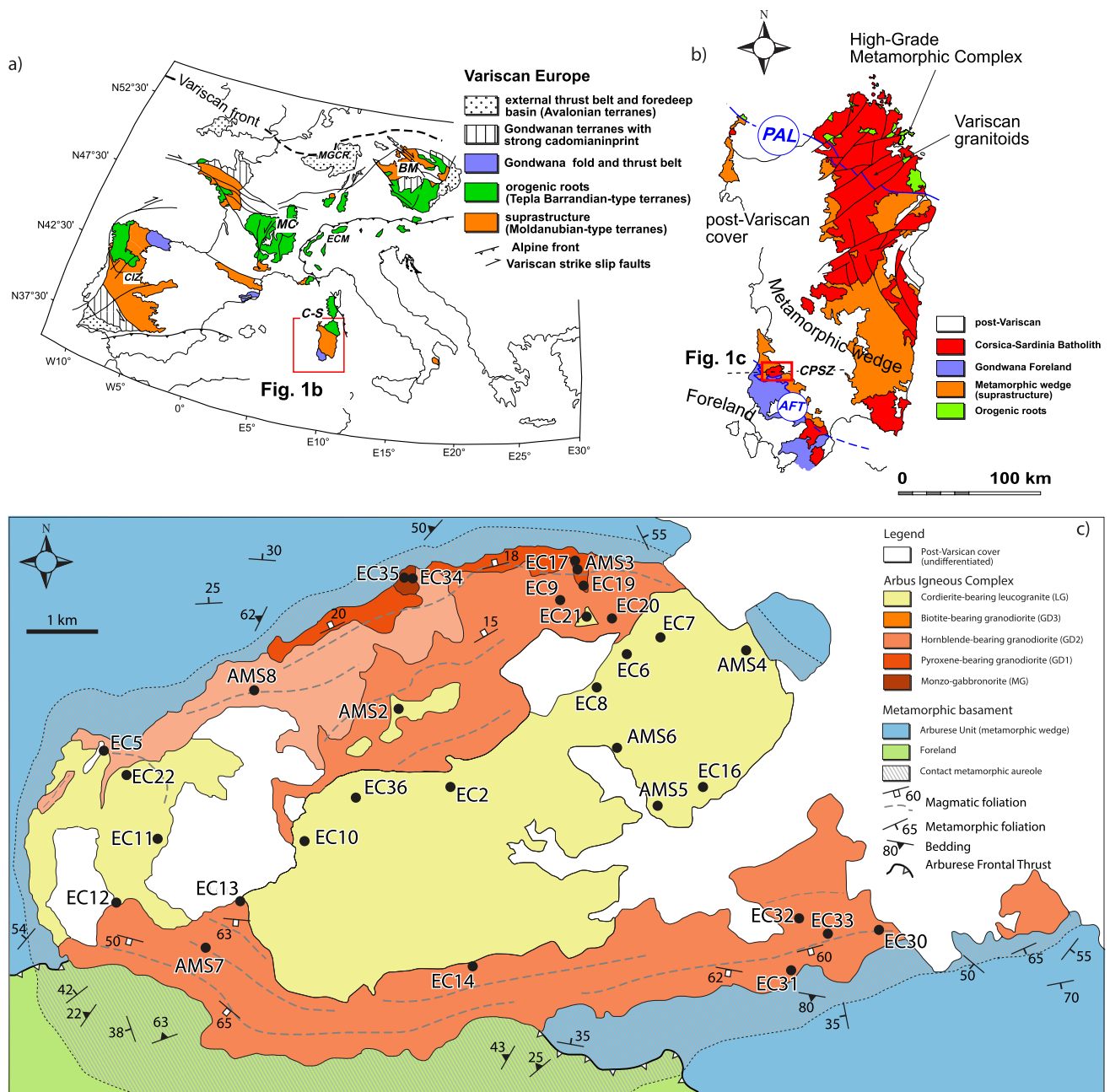


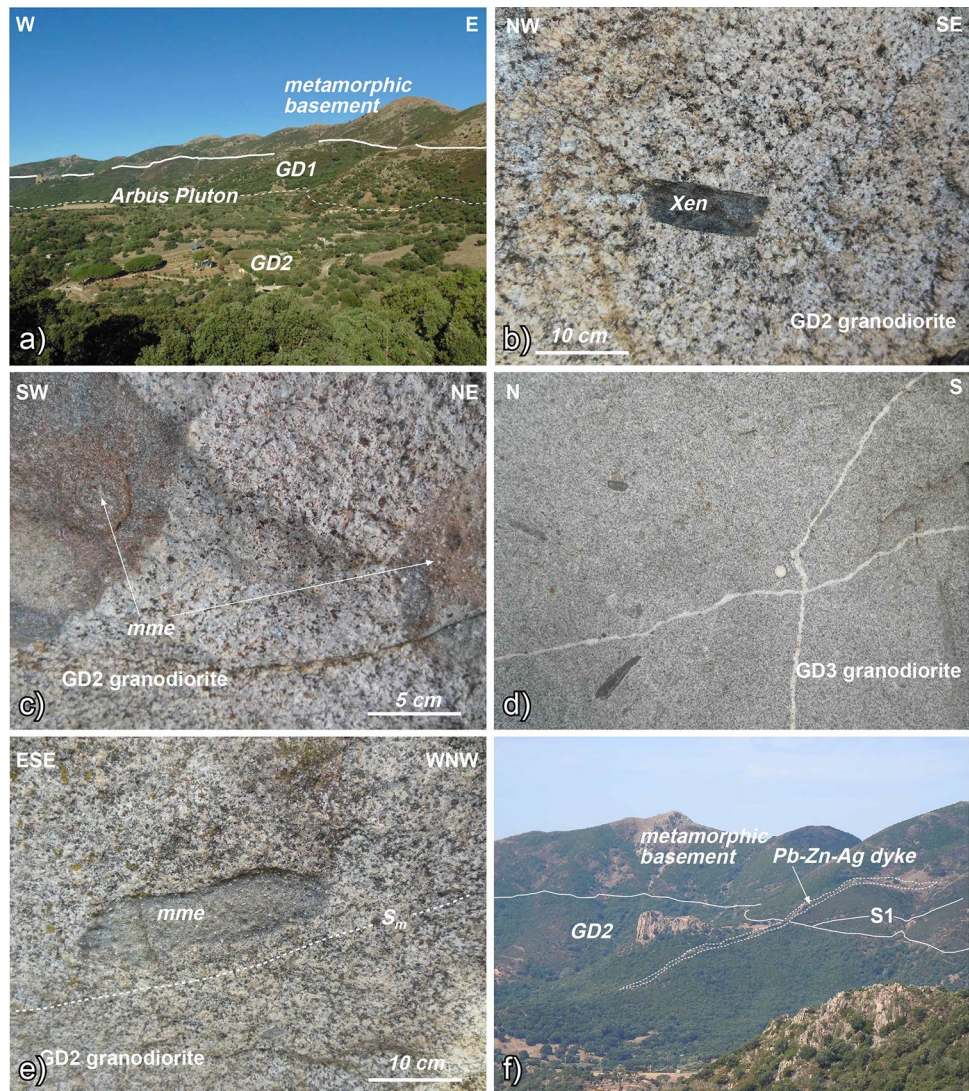
Fig. 1 Schematic geological map of late-Variscan Arbus pluton (southwestern Sardinia, Italy), simplified after Casini et al. (2015a) and Cuccuru et al. (2016). **a** Structural scheme of Variscan Europe; BM, Bohemian Massif; ECM, External Crystalline Massifs; MC, Massif Central; C-S, Corsica-Sardinia; CIZ, Central Iberian Zone;

MGCR, Mid German Crystalline Rise. **b** Simplified geological map of Sardinia Batholith; AFT, Arburese Frontal Thrust, CPSZ, Capo Pecora Shear Zone, PAL, Posada-Asinara Line. **c** Geological map of Arbus pluton with structural data and AMS sites location

by pale green Fe-chlorite) which become more frequent in LG1 and LG3 granites. In these latter rock-types, Fe-cordierite occurs as sub-vertical swarms of sub-rounded centimetric clots showing graphic textures with quartz. Finally, according to Secchi et al. (1991) and Secchi and D'Antonio (1996), the whole data set indicates that all

magma batches evolved from a common mantle-derived olivine-bearing magma source, assimilating variable amounts of crustal component.

Fig. 2 Field structures of the Arbus Pluton: **a** overview of the northern pluton margin showing nearly horizontal contact between GD1 granodiorites and metamorphic rocks (thick solid line); the dashed line marks the gently dipping contact between GD1 and GD2 granodiorites; **b** metamorphic xenolith (Xen) within fine-grained GD2 granodiorite, northern margin of the pluton; **c** rounded to elliptical micro-granular mafic enclaves (mme), southern margin of the pluton; **d** small metamorphic xenoliths with weak preferred orientation within GD3 granodiorites, central part of the pluton, **e** close-up of GD2 granodiorite from the southern margin of the pluton showing a pervasive E–W magmatic foliation (S_m) marked by the preferred orientation of plagioclase and pyroxene crystals and elongate micro-granular mafic enclaves (mme), **f** close-up of (a) showing a sub-vertical late magmatic Zn–Pb–Ag dyke emplaced within a radial fracture crossing through the pluton–metamorphic basement contact, northern margin of the pluton



Analytical methods

Structural analysis

The fabric of the pluton and its internal geometry defined by the magmatic foliation and lineation have been investigated by field structural analysis using the Shape Preferred Orientation (SPO) of micro-granular mafic enclaves, metamorphic xenoliths and biotite schlieren (Vernon et al. 2004; Paterson et al. 2019). These macroscopic flow markers are widespread throughout the pluton except within the leucogranites, which show no perceptible fabric. The crystallographic preferred orientation (CPO) of large idiomorphic plagioclase feldspar and amphibole has been also determined in a few relatively coarse-grained domains of granodiorite units to complement information on magmatic fabric pattern. The deformation feature characterizing the various domains of the pluton have been investigated by microstructural analysis

of selected samples. Polished thin sections were oriented parallel to XZ planes of the finite strain ellipsoid defined by the SPO and CPO.

Anisotropy of magnetic susceptibility (AMS)

Samples for AMS measurements were collected at 31 selected outcrops evenly distributed over about 67 km² area (Fig. 1c). Sampling stations were characterized by the absence of pervasive fractures and were located far from faults, alteration fronts and Fe-cordierite rich vertical swarms in LG rocks. Samples were collected by extracting in situ-oriented pieces of rocks. From each site, 6 to 12 cylindrical cores were drilled from oriented rock pieces using a vertical column drilling machine. The low-field AMS at room temperature was measured with an AGICO KLY-3S susceptibility bridge in the Paleomagnetic laboratory of Roma Tre University (Italy). The anisotropy measurements

Table 1 Summary of main petrographical features for intrusive rocks from Arbus igneous complex^a

| Fundamental phases | Accessory phases | ϵNd_{304} | $\delta^{18}\text{O}_{\text{SMOW}}\%$ | Age (Ma) |
|---|---|---------------------------|---------------------------------------|----------|
| <i>Cordierite-bearing leucogranites</i> (LG1, LG2 and LG3) | | | | |
| Kfs + Qz + Na-Pl + Fe-Bt ± Fe-Crdt | Xen + Mon + Zir + Aln and rare: Ilm, Ap, Fl, Tur, Thor, Uran, Sulph | -6.60 | +11.17 ± 0.50 | 308 ± 1 |
| <i>Granodiorites</i> | | | | |
| Pl + Kfs + Qz + Bt + Crdt ± Cpx _{on pl} ± Fe-Crdt (GD3) | Zir + Ap + All + Ilm | -6.60 | +10.23 ± 0.27 | 304 ± 1 |
| Pl + Qz + Kfs + Bt ± Opx _{pl} ± Cpx _{pl} (GD2) | and Xen + Mon + Tit + Uran | -7.79 | +9.54 ± 0.26 | |
| or (southern zones) Pl + Qz + Kfs + Bt + Hbl (GD2) | | -7.25 | +9.14 ± 0.50 | |
| Pl + Bt + Opx + Cpx + Qz + Kfs ± Crdt (GD1) | | | | |
| <i>Leuco quartz-monzo gabbronorites</i> (MG) | | | | |
| Ca-Pl + Bt + Opx + Cpx + Qz + Kfs ± Ol | Ilm + Ap + Zir + All | -5.87 | +8.09 ± 0.13 | |

^aIntegrated after Secchi et al. (1991) and Secchi and D'Antonio (1996). Radiometric ages reported in boldface and italic refer to U/Pb method on single zircon from GD1 granodiorites (Cuccuru et al. 2016) and ⁴⁰Ar/³⁹Ar on late-stage white mica from LG3 leucogranites (Boni et al. 2003), respectively. Other radiometric ages refer to Rb–Sr isochrones recalculated after Secchi et al. (1991) for MG-GD3 and LG1-LG2 rock-sequences. Rocks are commonly medium to fine-grained and show hypidiomorphic granular or porphyritic textures often with graphic textures and were classified according to Le Bas and Streckeisen (1991) constraints. Mineral abbreviations according to Kretz (1983) and Whitney and Evans (2010): Pl = plagioclase; Qz = quartz; Kfs = K-feldspar; Ol = olivine; Opx = orthopyroxene (hypersthene); Cpx = clinopyroxene (augite); Bt = dark mica; Hbl = green hornblende; Crdt = cordierite (sekaninaite); Ms = white mica; Ilm = ilmenite; Ap = apatite; Aln = allanite; Zir = zircon; Xen = xenotime; Mon = monazite; Fl = fluorite; Tit = titanite; Thor = thorite; Uran = uraninite; Sulph = sulfides e Tur = tourmaline of schorl composition (Bosi et al. 2018). Average composition of plagioclase ranges from labradorite in MG monzo-gabbronorites to oligoclase in leucogranites whereas in same rocks, dark micas range from Fe-biotite to siderophyllite. Other abbreviations as reported in Fig. 1

at the site levels were evaluated using Jelinek's (1977) statistics.

AMS is defined by a second rank tensor and represented geometrically by an ellipsoid in which the greatest intensity of magnetization is induced along the long axis K_{max} and the weakest intensity along the short axis K_{min} (with principal axes $K_{\text{max}} > K_{\text{int}} > K_{\text{min}}$). Several parameters have been defined both for the quantification of the magnitude of anisotropy and for defining the shape of the ellipsoid (Jelinek 1981; Hrouda 1982). The magnetic lineation L ($K_{\text{max}}/K_{\text{min}}$) is defined by the orientation of K_{max} , while the magnetic foliation F ($K_{\text{int}}/K_{\text{min}}$) is defined as the plane perpendicular to K_{min} . The anisotropy degree and the shape factor are expressed by the parameter Pj and T, respectively (Table 2, Jelinek 1981).

Thermal modelling

Several parameters control the cooling history of plutons and the development of related contact metamorphic aureole, including: (i) the ratio between magma and country rock temperatures, (ii) melt injection rate and frequency of injections (Annen et al. 2006; Annen 2011). The effectiveness of each parameter is evaluated through a suite of 2D numerical experiments that simulate different growth histories of Arbus pluton using a purely thermal version of the finite difference code evp2d (Casini 2012; Casini et al. 2013; Maino et al. 2015, 2020; Casini and Maino 2018). In the first set of parametric experiments, we evaluate the pluton cooling rates for different initial crustal geothermal profile. The second group

of experiments addresses the effect of melt injection rate and the frequency of injections. In the remainder of this section, we summarize the basic aspects of our modelling strategy focusing on the experimental setup adopted to reproduce the growth and cooling history of the pluton. Further details about the algorithm and numerical approximations used by the code can be found in Casini and Maino (2018).

Mathematical background

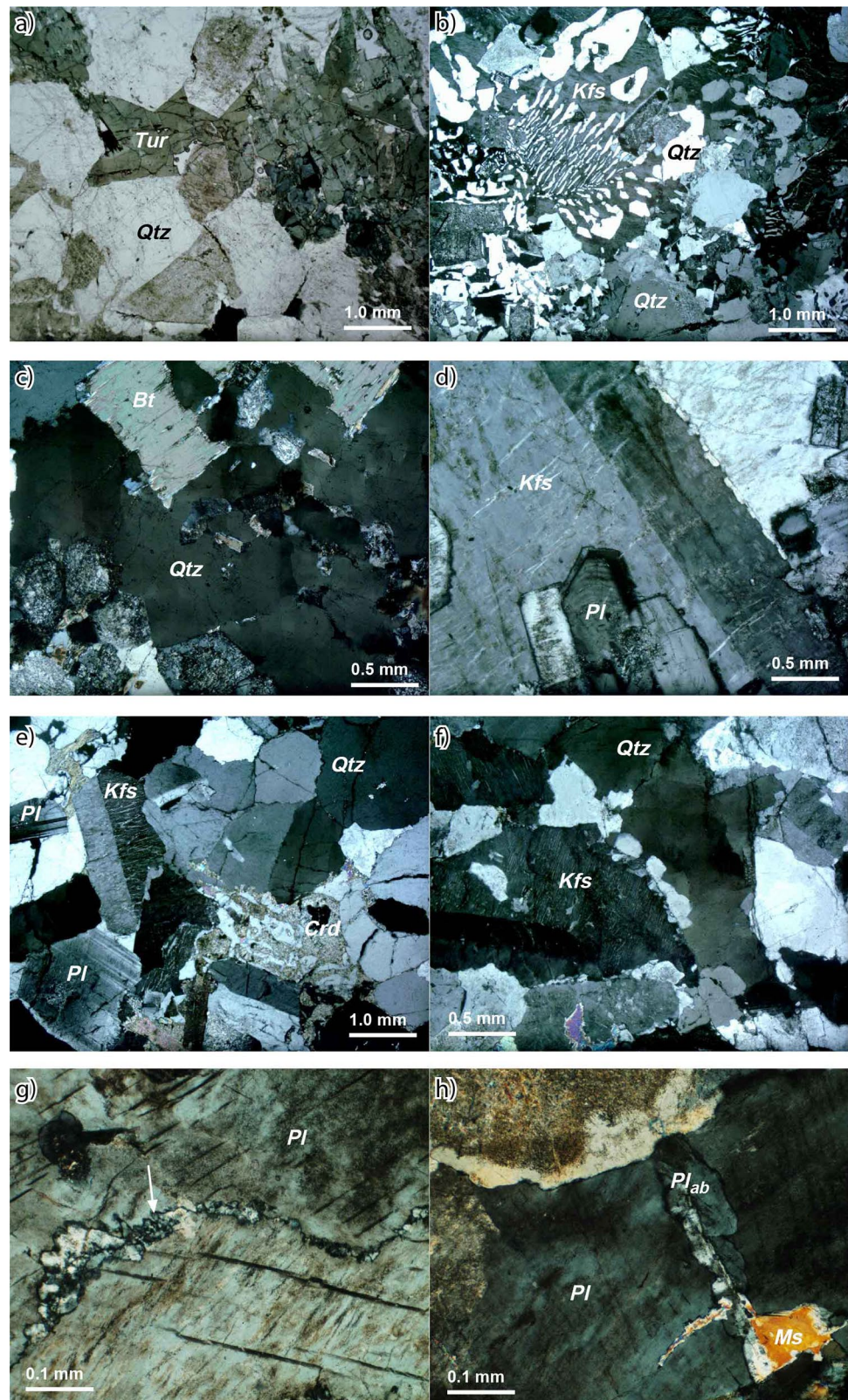
The lagrangian heat equation is formulated in 2D space assuming temperature-dependent thermal conductivity (Vosteen and Schellschmidt 2003; Whittington et al. 2009) and heat sources:

$$\rho C_p \frac{DT}{Dt} = \frac{\partial q_i}{\partial x_i} + H_r + H_L \quad (1)$$

$$q_i = \frac{\partial}{\partial x_i} \left(k \frac{\partial T}{\partial x_i} \right) \quad (2)$$

where DT/Dt is the Lagrangian time-derivative of temperature, ρ is density ($[\text{kgm}^{-3}]$) and H_r represents the volumetric heat production rate ($[\text{Wm}^{-3}]$) due to the decay of radioactive elements. The parameters C_p and k are specific heat capacity ($[\text{Jkg}^{-1} \text{K}^{-1}]$) and thermal conductivity ($[\text{Wm}^{-1} \text{K}^{-1}]$), respectively. This latter parameter is expressed as $k = \kappa \rho C_p$ where κ is thermal diffusivity ($[\text{m}^2\text{s}^{-1}]$). Both k and C_p are formulated as temperature-dependent parameters according

Fig. 3 Microstructure of the Arbus pluton: **a** Interstitial greenish tourmaline on LG3 leucogranites, plane polarized light, northern margin of the pluton, **b** graphic texture of LG3 leucogranites, crossed polarizers, northern margin of the pluton, **c** chessboard texture of quartz in GD3 granodiorites, crossed polarizers, northern margin of the pluton, **d** flame perthite, in GD3 granodiorites, north-central part of the pluton, **e** Fe-cordierite (now altered)-quartz graphic intergrowths on LG1 leucogranites, crossed polarizers, pluton core, **f** chessboard texture of quartz and late-stage white-mica + feldspar assemblage on LG2 leucogranites, crossed polarizers, central part of the pluton, **g** incipient micro-shear zone (white arrow) developed at plagioclase-plagioclase grain-boundary, GD2 granodiorites, southern margin of the pluton, **h** syn-magmatic fracture of plagioclase filled by muscovite + albitic plagioclase, GD2 granodiorites, southern margin of the pluton. Mineral abbreviation list as reported in Table 1



to the equations of Whittington et al. (2009). The term H_L is the latent heat of crystallization ($[Jkg^{-1}]$). This latter is computed as function of the melt fraction M and its contribution

decreases linearly from a value of $3 \times 10^5 J kg^{-1}$ corresponding to a completely liquid magma to zero once crystallization is complete (Annen 2009). As a first approximation the

Table 2 AMS data from the Arbus pluton (southwestern Sardinia, Italy)

| Samples | Sampling locality | Latitude | Longitude | Map reference | <i>n</i> | <i>K_m</i> | <i>L</i> | <i>F</i> | <i>P_j</i> | <i>T</i> | D.I (<i>K_{max}</i>) | D.I (<i>K_{min}</i>) | E(1–2) |
|------------|--------------------|------------|-----------|------------------------|----------|----------------------|----------|----------|----------------------|----------|--------------------------------|--------------------------------|--------|
| EC34 (MG) | Punta C. Masonis | N39°32'14" | E8°34'19" | 546I (Gùspini) | 7 | 75.3 | 1.033 | 1.006 | 1.043 | -0.7 | 190.5 | 297.73 | 8 |
| EC35 (MG) | Punta C. Masonis | N39°32'14" | E8°34'16" | 546I (Gùspini) | 9 | 110 | 1.001 | 1.035 | 1.041 | 0.945 | 237.61 | 92.24 | 71 |
| AMS3 (GD1) | Genna Sciria | N39°32'26" | E8°36'14" | 546I (Gùspini) | 21 | 32.2 | 1.004 | 1.002 | 1.006 | -0.352 | 294.2 | 202.53 | 16 |
| EC17 (GD1) | Genna Sciria | N39°32'26" | E8°36'13" | 546I (Gùspini) | 9 | 23.9 | 1.005 | 1.000 | 1.006 | -0.816 | 264.0 | 354.38 | 21 |
| EC19 (GD1) | Punta Ruinas | N39°32'21" | E8°36'12" | 546I (Gùspini) | 8 | 28.9 | 1.006 | 1.006 | 1.012 | 0.041 | 23.18 | 270.49 | 6 |
| AMS7 (GD2) | Grutzu | N39°29'08" | E8°32'12" | 546II (Gonnosfanàdiga) | 9 | 19.0 | 1.003 | 1.008 | 1.011 | 0.388 | 239.54 | 18.29 | 31 |
| EC9 (GD2) | Genna Ruinas | N39°32'08" | E8°36'08" | 546I (Gùspini) | 8 | 23.2 | 1.001 | 1.012 | 1.015 | 0.798 | 86.12 | 339.54 | 61 |
| EC14 (GD2) | Case Marigosa | N39°29'09" | E8°35'14" | 546II (Gonnosfanàdiga) | 10 | 9.5 | 1.020 | 1.007 | 1.028 | -0.464 | 195.7 | 290.35 | 10 |
| EC30 (GD2) | Santa Severa | N39°29'07" | E8°39'10" | 546II (Gonnosfanàdiga) | 8 | 23.9 | 1.008 | 1.011 | 1.019 | 0.148 | 270.18 | 3.10 | 14 |
| EC31 (GD2) | Monte Oliastu | N39°28'58" | E8°38'19" | 546II (Gonnosfanàdiga) | 10 | 23.2 | 1.011 | 1.006 | 1.017 | -0.298 | 103.17 | 357.40 | 11 |
| EC32 (GD2) | Cuccuru Genna | N39°29'29" | E8°38'22" | 546II (Gonnosfanàdiga) | 10 | 18.0 | 1.001 | 1.010 | 1.012 | 0.823 | 223.40 | 89.40 | 67 |
| EC33 (GD2) | Cuccuru Genna | N39°29'23" | E8°38'25" | 546II (Gonnosfanàdiga) | 6 | 14.2 | 1.078 | 1.037 | 1.121 | -0.351 | 21.22 | 236.64 | 7 |
| EC13 (GD2) | Ponte Riu Marronis | N39°29'51" | E8°32'23" | 546II (Gonnosfanàdiga) | 9 | 11.7 | 1.011 | 1.011 | 1.022 | 0.010 | 99.5 | 356.71 | 13 |
| EC20 (GD2) | Cuccureddu | N39°32'03" | E8°36'19" | 546I (Gùspini) | 7 | 21.5 | 1.006 | 1.018 | 1.025 | 0.486 | 20.14 | 113.12 | 18 |
| AMS8 (GD3) | Genna de su Bentu | N39°31'25" | E8°32'54" | 546I (Gùspini) | 8 | 12.5 | 1.001 | 1.005 | 1.007 | 0.601 | 192.5 | 88.72 | 46 |
| AMS5 (LG1) | Baratzu | N39°30'29" | E8°37'02" | 546I (Gùspini) | 9 | 5.5 | 1.003 | 1.026 | 1.030 | 0.767 | 348.28 | 145.60 | 51 |
| EC2 (LG1) | Genna isPiscis | N39°30'32" | E8°34'59" | 546I (Gùspini) | 14 | 3.1 | 1.009 | 1.022 | 1.032 | 0.415 | 47.3 | 142.62 | 18 |
| EC10 (LG1) | Su Sparau | N39°30'03" | E8°33'21" | 546II (Gonnosfanàdiga) | 7 | 4.62 | 1.006 | 1.013 | 1.020 | 0.414 | 254.43 | 18.31 | 38 |
| EC16 (LG1) | Baratzu | N39°30'33" | E8°37'10" | 546I (Gùspini) | 9 | 5.4 | 1.016 | 1.044 | 1.063 | 0.463 | 57.16 | 292.64 | 19 |
| EC36 (LG1) | Monte Spartau | N39°30'23" | E8°33'54" | 546I (Gùspini) | 9 | 5.49 | 1.002 | 1.027 | 1.033 | 0.856 | 110.2 | 7.81 | 74 |
| EC22 (LG2) | Genna Sartania | N39°30'42" | E8°31'43" | 546I (Gùspini) | 6 | 6.0 | 1.011 | 1.022 | 1.034 | 0.333 | 100.3 | 336.85 | 16 |
| AMS2 (LG2) | Punta Cugui | N39°31'14" | E8°34'22" | 546I (Gùspini) | 12 | 5.5 | 1.004 | 1.015 | 1.020 | 0.583 | 218.11 | 349.73 | 47 |
| AMS4 (LG2) | Sa Tella | N39°32'00" | E8°37'44" | 546I (Gùspini) | 9 | 3.8 | 1.003 | 1.019 | 1.024 | 0.708 | 51.24 | 215.65 | 51 |
| EC5 (LG2) | Pitzinurri | N39°31'03" | E8°30'55" | 546I (Gùspini) | 11 | 8.9 | 1.010 | 1.006 | 1.016 | -0.255 | 269.33 | 144.41 | 16 |
| EC6 (LG2) | Monti Mannu | N39°31'50" | E8°36'48" | 546I (Gùspini) | 10 | 2.24 | 1.026 | 1.099 | 1.136 | 0.568 | 267.11 | 57.77 | 23 |
| EC8 (LG2) | Punta Conca Malu | N39°31'25" | E8°36'18" | 546I (Gùspini) | 9 | 4.29 | 1.004 | 1.025 | 1.031 | 0.748 | 211.2 | 47.88 | 64 |
| EC11 (LG2) | Scrabaxius | N39°30'04" | E8°31'49" | 546II (Gonnosfanàdiga) | 9 | 3.31 | 1.015 | 1.092 | 1.117 | 0.715 | 32.2 | 291.80 | 22 |
| EC21 (LG2) | Cuccureddu | N39°31'58" | E8°36'18" | 546I (Gùspini) | 10 | 6.1 | 1.004 | 1.018 | 1.024 | 0.602 | 286.3 | 175.83 | 33 |
| EC7 (LG3) | Monti Mannu | N39°31'52" | E8°37'00" | 546I (Gùspini) | 6 | 2.71 | 1.016 | 1.028 | 1.045 | 0.286 | 311.6 | 146.83 | 11 |
| EC12 (LG3) | Pozzo Edoardo | N39°29'26" | E8°30'37" | 546II (Gonnosfanàdiga) | 8 | 63.6 | 1.032 | 1.641 | 1.380 | 0.880 | 297.2 | 42.81 | 62 |
| AMS6 (π) | Baratzu | N39°30'46" | E8°36'43" | 546I (Gùspini) | 8 | 5.6 | 1.006 | 1.014 | 1.020 | 0.396 | 313.13 | 108.76 | 38 |

n = number of analyzed specimen for each sampling site. D.I (*K_{max}*) and D.I (*K_{min}*) refer to azimuth and plunge declination and inclination of maximum and minimum axis of magnetic susceptibility, respectively. *K_m* = (*K_{max}* + *K_{int}* + *K_{min}*)/3 is expressed as 10⁻³ SI units and refer to the average value of magnetic susceptibility. *L* = *K_{max}*/*K_{int}* (magnetic lineation); *F* = *K_{int}*/*K_{min}* (magnetic foliation); *P_j* = exp{2[(*η*1 - *η*2) + (*η*3 - *η*2)]²}^{1/2} (corrected anisotropy degree); *T* = 2(*η*2 - *η*3)/(*η*1 - *η*3) - 1 (form factor according to Jelínek, 1981); *η*1 = ln*K_{max}*; *η*2 = ln*K_{int}*; *η*3 = ln*K_{min}*; *η* = (*η*1 + *η*2 + *η*3)/3; *e*₁₋₂ = semi-angle of the 95% confidence ellipses around the principal susceptibility axes. Map references refer to samples position on IGM official map of Italy at 1/25000 scale. Sample AM26 (π) refer to an acidic dike crosscutting LG1 granites. Abbreviations for intrusive units, as reported in Fig. 1

melt fraction is assumed to change linearly with temperature according to the relations (Gerya and Yuen 2003; Burg and Gerya 2005):

$$\begin{cases} M = 0 \rightarrow T \leq T_S \\ M = \frac{(T-T_S)}{(T_L-T_S)} \rightarrow T_S < T < T_L \\ M = 1 \rightarrow T \geq T_L \end{cases} \quad (3)$$

where T is the actual temperature of the marker, T_S ([K]) and T_L ([K]) are the solidus and liquidus temperature of magma.

The spatial coordinates are denoted by x_i , the index $i = 1, 2$, and repeated indices denote summation according to the Einstein summation convention. The heat equation is solved using a fully implicit Crank–Nicholson algorithm

which ensures second-order accuracy both in time and space (Crank and Nicholson 1947). Advection due to incremental injection of magma batches is accounted for by tracing the displacements of material points using a large number of Lagrangian markers, up to 2.4 million in the high-resolution experiments (Casini and Maino 2018; Maino et al. 2020). As the model is purely thermal, advection is simulated in a simplified way. Each magma batch is represented in 2D as a pseudo-elliptical body composed of four quadrants that have minor and major semi-axis of length a_i , b_i , respectively (Fig. 4b). The pluton builds up progressively by adding N pulses of equal area; thus, the final area of the pluton A_p is defined summing over a prescribed number of magmatic pulses, N :

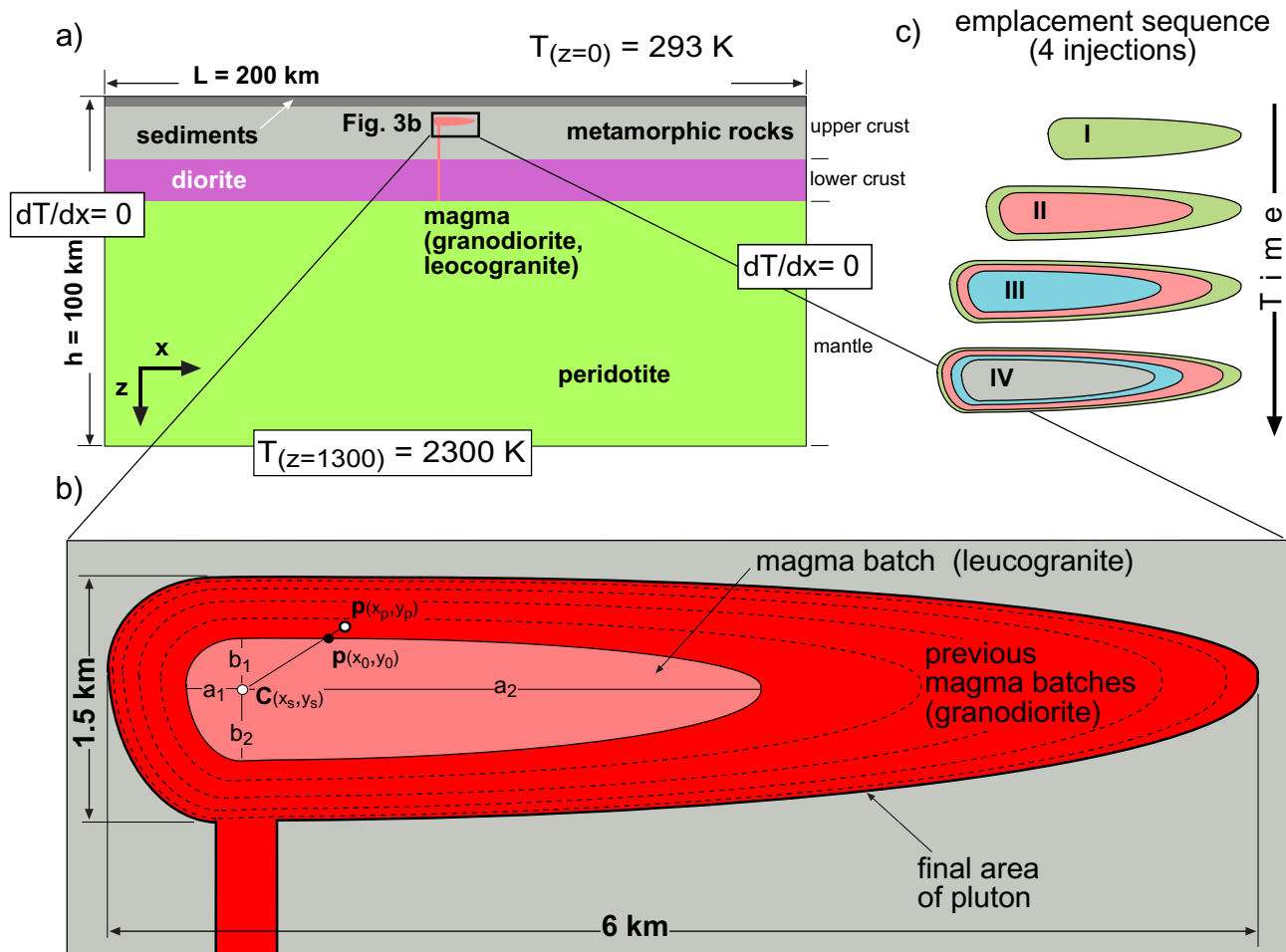


Fig. 4 Model setup: **a** Composition and geometry of the model lithosphere used for thermal experiments (see Table 3 for details of physical properties and thickness of the various layers). The thermal boundary conditions are specified as insulating lateral boundaries, Dirichlet (constant $T=293.15$ K) upper boundary, and external Dirichlet (constant $T=2300$ K) at the lower boundary. The site of plu-

ton emplacement is indicated; **b** Close-up of the pluton geometry showing the displacement of material points after emplacement of a magma batch, the white dot of coordinates x_p, y_p indicates the new position of point p of initial coordinates x_0, y_0 (black dot), **c** example of a 4-pulses sequence of injections

Table 3 Experimental setup and material parameters

| Composition | Thickness (m) | κ (m ² s ⁻¹) | ρ (kg m ⁻³) | Hr (Wm ⁻³) | Cp (Jkg ⁻¹ °C ⁻¹) | T_{Liq} (K) | T_{Sol} (K) | Reference |
|-------------------|---------------|--|------------------------------|------------------------|--|---------------|---------------|-----------|
| Lithosphere | | | | | | | | |
| Sediment | 3000 | $k_{(T<846)} = 567.3/T - 0.062$, $k_{(T>846)} = 0.732 - 0.000135 T$ | 2500 | $1.80 \cdot 10^{-6}$ | $Cp_{(T<846)} = 199.5 + 0.0857 T - 5 \times 10^{-6} T^2$ | | | a,b |
| Metamorphic rocks | 15,000 | | 2700 | $2.20 \cdot 10^{-6}$ | $Cp_{(T>846)} = 229.32 + 0.0323 T - 47.9 \times 10^{-6} T^2$ | | | a,b,c |
| Diorite | 12,000 | | 2900 | $8.00 \cdot 10^{-5}$ | | | | a,b,d |
| Pertidotite | 70,000 | $k = 0.73 + 1.293/(T + 77)$ | 3300 | $5.00 \cdot 10^{-8}$ | 1000 | | | a |
| Pluton | | | | | | | | |
| Granodiorite | Variable | $k_{(T<846)} = 567.3/T - 0.062$, $k_{(T>846)} = 0.732 - 0.000135 T$ | 2750 | $1.50 \cdot 10^{-6}$ | $Cp_{(T<846)} = 199.5 + 0.0857 T - 5 \times 10^{-6} T^2$ | 1193 | 1073 | a,b |
| Leucogranite | | | 2680 | $2.50 \cdot 10^{-6}$ | $Cp_{(T>846)} = 229.32 + 0.0323 T - 47.9 \times 10^{-6} T^2$ | 1123 | 993 | a,b,c |

^aWhittington et al. (2009)

^bVilà et al. (2010)

^cPuccini et al. (2014)

^dBurg and Gerya (2005)

$$A_p = \sum_{i=1}^N \sum \frac{\pi a_i b_i}{4} \tag{4}$$

The emplacement of magmatic pulses is evenly distributed over a given time interval which depends on the prescribed frequency of injection ω [1/s], defined as the time interval between two consecutive magma batches. Given that emplacement of each magma batch is represented as an instantaneous process, the melt injection rate \dot{I} [m²/s] is defined in 2D as the time-derivative of the net increase in area due to emplacement of the i th magma batch as:

$$\dot{I} = \frac{\partial \sum \frac{\pi a_i b_i}{4}}{\partial t} \tag{5}$$

After emplacement of each magma batch the country rocks and previous magma batches are displaced following a radial displacement field (Fig. 4b) directed outward from point C of coordinate x_s, y_s representing the centroid of the pluton (e.g., Caricchi et al. 2012), so that the new position (x_p, y_p) of a material point p of coordinates x_0, y_0 is calculated as follows:

$$\begin{cases} x_p = -B \pm \frac{\sqrt{B^2 - 4AC}}{2A} \\ y_p = \alpha p(x_0) + q \end{cases} \tag{6}$$

$$A = b_i^2 + a_i^2 \alpha^2 \tag{7}$$

$$B = 2(a_i^2 \alpha q - x_s b_i^2 - y_s a_i^2 \alpha) \tag{8}$$

$$C = 2(b_i^2 x_s + a_i^2 q^2 + a_i^2 y_s^2 - a_i^2 y_s) - a_i^2 b_i^2 \tag{9}$$

where α and q define the slope and intercept of the line connecting point p to the centroid of the magma batches, respectively, and the other variables have been already defined. In all experiments, the contact metamorphic aureole is characterized by capturing either the maximum T recorded within 10 m from either the southern or northern borders of the pluton and the maximum distance reached by the 600 K isotherm, indicated respectively as $T_N, T_S,$ and W_N and W_S . This temperature is used to compare experimental results with field observation, as the 600 K isotherm roughly corresponds to the onset of muscovite-forming reactions in low-P metapelites (i.e., Wei et al. 2004). Besides, we also extracted the total time t_c [Myr] required to completely cool the whole magmatic system (i.e., the contact metamorphic aureole and the core of the pluton) below 600 K.

Experimental setup and boundary conditions

The proposed model consists of a rectangular domain 200 km-wide that simulates a 30 km-thick crust (18 km felsic upper crust, and 12 km mafic lower crust) overlying 70 km-thick lithospheric mantle (Fig. 4a). The full details of the experimental setup and thermal properties of the different model materials are provided in Table 3 and Fig. 4a,b. The vertical boundaries are assumed to be insulating, whereas a Dirichlet boundary condition ($T(z_0) = 293.15$ K) is imposed at the upper boundary of the model which corresponds to the topographic surface (Fig. 4). A constant 2300 K temperature is prescribed at an external lower boundary set at 1300 km depth, far below the bottom of the model, to minimize the numerical artifacts due to the choice of restrictive boundary conditions (Fig. 4). Equation (1) is discretized using an Eulerian grid composed of 100 by 200 irregularly spaced nodes. This configuration corresponds to a maximum resolution of about 50 m in the central domain representing the pluton and its surrounding contact metamorphic aureole. Before running the parametric experiments to test the effect of variable injection rate and injection frequency, we evaluate the sensitivity of the model to the grid size in a suite of 5 experiments using a variable grid size ranging from 10 to 500 m in the highest resolution domain, and 5 magma batches emplacing every 0.025 Myr resulting into a total lifetime of the magmatic system of 0.1 Myr (Table 4). The sensitivity tests show that the temperature pattern does not change for a grid size finer than 50 m, thus in the remaining experiments we use a cell size of 50 m in the central upper part of the model to ensure an optimal resolution for the emplacement site and the contact metamorphic aureole. A total of 34 numerical experiments, including the sensitivity tests (AR00a-e, Table 4), were ran to reproduce the cooling of the Arbus pluton and the development of the related contact metamorphic aureole. Field structural data and geological constraints indicate that the pluton might be approximated as an asymmetric 1500 m-thick and 6000 m-wide tabular intrusion with a cross-sectional area of about 7 km² (Secchi et al. 1991; Cuccuru et al. 2016). The compositional variability of the pluton is reproduced in a simplified way injecting a variable number of magma batches of either granodioritic or leucogranitic composition. In all experiments the sequence of emplacement is from granodiorite to leucogranite resulting in a final proportion of felsic to relatively mafic terms of about 0.25, consistent with field structural analysis and AMS (Secchi et al. 1991; Cuccuru et al. 2016; this work). The emplacement depth and the solidus (T_S) and liquidus (T_L) temperatures of compositionally-distinct magma batches is deduced from Al-in hornblende in GD granodiorites and CIPW normative mineral contents (i.e. quartz and albite plus orthoclase) of LG granitic rocks according to Yang's (2017) constraints (Secchi et al. 1991; Bosi et al. 2019).

The thermal properties of different magma batches are listed in Table 3. Incremental accretion is reproduced assuming a dyke propagation model with instantaneous advection of magma along perfectly vertical trajectories, which is a reasonable approximation for incrementally accreted shallow-crustal plutons or volcanic complexes (Annen et al. 2006; Albert et al. 2020). This implies that our experiments explicitly neglect conductive heat loss during the ascent of magma, providing a maximum estimate for the dimension and persistence of the contact metamorphic aureole. Under these assumptions, the major parameters controlling the thermal evolution are the temperature of melt, the initial (pre-emplacment) temperature of country rocks, the melt injection rate \dot{I} and the frequency of magmatic injections, ω . The Arbus pluton preserves evidence for extensive compositional homogenization within each magma batch, as well as ductile and gradational contacts between the different batches. Thus, we limit the melt injection frequencies to values lower than $1.2 \times 10^{-10} \text{ s}^{-1}$ in all experiments to avoid complete crystallization before emplacement of the next magma batch (Table 4). Given a general sill-shaped geometry, we calculate the pluton emplacement rate ψ [m/s, Table 4] as the time-averaged vertical growth rate of the sill (Annen 2011). In the absence of convection and neglecting the latent heat of crystallization, the mean timescale for cooling (Δt , [s]) a single magma batch of thickness h [m] can be roughly estimated from the 1D diffusion equation, provided that the width of the magma batch exceeds its thickness so that the overall geometry approximates that of a tabular intrusion:

$$\Delta t \sim \frac{\left(\frac{h}{2}\right)^2}{\kappa} \quad (10)$$

For typical κ values of $1.1 \times 10^{-6} \text{ m}^2\text{s}^{-1}$ (Whittington et al., 2009), Eq. (10) implies that the minimum frequency of magmatic injections required to prevent complete cooling of 10–375 m-thick sills during incremental construction of a tabular intrusion ranges between about $4.4 \times 10^{-8} \text{ s}^{-1}$ and $3.12 \times 10^{-11} \text{ s}^{-1}$, respectively (i.e., exp AR27 and AR15, Table 3). The effect of the initial temperature of country rocks is evaluated in a first set of parametric experiments (AR01a-g, Table 4) changing the pre-emplacment steady-state geothermal profile. We tested eight different thermal configurations that correspond to cold (12, 15 K km⁻¹), intermediate (18, 20, 22, 25 and 30 K km⁻¹) and hot (40 K km⁻¹) linear-sectioned crustal geotherms in the middle crust and sedimentary layer, i.e., within the first 18 km of the model domain. The temperature of the Moho is set to 1170 K in all experiments; thus a hot crust corresponds to gentle geothermal gradient in the lower crust. For the purpose of demonstration, in these experiments we assume a simple incremental growth history consisting of periodic injection of 5300 m-thick sills, corresponding to the main

Table 4 Summary of experimental results

| Experiment | Pluton growth model | | | Contact aureole | | | | t_f (Myr) | t_c (Myr) | Note | |
|------------|----------------------------|--------------------------|-----------------------------|-------------------------------------|------------------------------|-----------|-----------|-------------|-------------|-------|--|
| | T ($^{\circ}\text{C}$) | N (Km^{-1}) | Ψ (ms^{-1}) | \dot{I} (m^2/s) | ω (s^{-1}) | W_s (m) | W_N (m) | | | | T_S (K) |
| AR00a | 25 | 5 | 4.75–10 | 2.23E–06 | 1.58E–12 | 1114.5 | 63.2 | 707 | 568 | 0.246 | 10 × 10 m grid |
| AR00b | | | | | | 1116.3 | 62.1 | 708 | 564 | 0.244 | 50 × 50 m grid |
| AR00c | | | | | | 1130.1 | 65.6 | 701 | 550 | 0.221 | 100 × 100 m grid |
| AR00d | | | | | | 1120.5 | 84.2 | 693 | 545 | 0.19 | 250 × 250 m grid |
| AR00e | | | | | | 1150.7 | 88.7 | 680 | 521 | 0.156 | 500 × 500 m grid |
| AR01 | 12 | | | | | 501.4 | 27 | 644 | 476 | 0.1 | Cold geotherm |
| AR01a | 15 | | | | | 641 | 22.9 | 678 | 492 | 0.321 | |
| AR01b | 18 | | | | | 826.1 | 43.2 | 695 | 512 | 0.404 | Intermediate geotherm |
| AR01c | 20 | | | | | 1018.4 | 73.1 | 724 | 546 | 0.508 | |
| AR01d | 22 | | | | | 1307 | 68 | 728 | 550 | 0.534 | |
| AR01e | 25 | | | | | 1540.8 | 71 | 784 | 586 | 0.59 | |
| AR01f | 30 | | | | | 1956.1 | 72 | 887 | 608 | 0.875 | |
| AR01g | 40 | | | | | 2445.3 | 75 | 958 | 675 | 1.65 | Hot geotherm |
| AR27 | 20 | 4 | 3.96E–09 | 9.33E–05 | 1.05E–11 | 1652.6 | 347 | 818 | 700 | 0.009 | Variable melt injection rate, 'high' frequency experiments |
| AR04 | | 8 | 1.98E–09 | 1.86E–05 | | 1480.8 | 312 | 761 | 686 | 0.021 | |
| AR18 | | 10 | 1.58E–09 | 7.46E–06 | | 1359.1 | 274 | 733 | 653 | 0.027 | |
| AR05 | | 16 | 9.90E–10 | 4.66E–06 | | 1107.4 | 124 | 721 | 626 | 0.045 | |
| AR6c | | 20 | 7.92E–10 | 3.73E–06 | | 1087.8 | 97 | 718 | 608 | 0.057 | |
| AR22 | | 32 | 4.95E–10 | 2.33E–06 | | 995.6 | 83 | 703 | 582 | 0.093 | |
| AR09 | | 50 | 3.16E–10 | 1.49E–06 | | 843.2 | 82.1 | 687 | 516 | 0.147 | |
| AR08 | | 80 | 1.98E–10 | 9.33E–07 | | 796.4 | 63.2 | 645 | 505 | 0.237 | |
| AR13 | | 120 | 1.32E–10 | 6.22E–07 | | 774 | 52.1 | 604 | 499 | 0.357 | |
| AR15 | | 150 | 1.05E–10 | 4.97E–07 | | 633.2 | 32.2 | 589 | 480 | 0.447 | |
| AR24 | | 4 | 2.37E–09 | 1.11E–05 | 6.33E–12 | 797.6 | 304.5 | 718 | 642 | 0.015 | Variable melt injection rate, 'low' frequency experiments |
| AR17 | | 10 | 9.50E–10 | 4.47E–06 | | 825.3 | 134.7 | 701 | 617 | 0.045 | |
| AR16 | | 30 | 3.16E–10 | 1.49E–06 | | 896.4 | 93.7 | 624 | 569 | 0.145 | |
| AR10 | | 50 | 1.90E–10 | 8.95E–07 | | 612.6 | 73.3 | 603 | 503 | 0.245 | |
| AR10b | | 100 | 9.50E–11 | 4.47E–07 | | 459.1 | 24.6 | 592 | 483 | 0.49 | |
| AR50 | | 25 | 1.90E–07 | 3.58E–05 | 1.26E–10 | 1785.6 | 286.2 | 894 | 601 | 0.006 | Variable frequency of magmatic injections |
| AR51 | | | 4.75E–08 | 8.95E–06 | 3.16E–11 | 1220.2 | 244.1 | 812 | 587 | 0.024 | |
| AR52 | | | 2.37E–08 | 4.47E–06 | 1.58E–11 | 994.2 | 94.1 | 735 | 550 | 0.048 | |
| AR53 | | | 9.50E–09 | 1.79E–06 | 6.33E–12 | 812.1 | 77.6 | 704 | 534 | 0.12 | |
| AR58 | | | 2.16E–09 | 4.07E–07 | 1.44E–12 | 721.5 | 62.1 | 682 | 501 | 0.528 | |
| AR60 | | | 1.53E–09 | 2.89E–07 | 1.02E–12 | 687.6 | 30.4 | 669 | 484 | 0.744 | |

magmatic units recognized in the field (Fig. 1c). The five sills emplace every 2.5×10^4 years to get a total emplacement time t_f of 0.1 Myr (Table 4), which is consistent with geological and geochronological constraints (Secchi et al., 1991; Cuccuru et al., 2016). These experiments imply a mean vertical accretion rate of about 2.37×10^{-9} ms $^{-1}$ and melt injection frequency of 1.27×10^{-12} s $^{-1}$ (Table 4). In a second set of parametric experiments using a fixed linear geothermal gradient of 20 K km $^{-1}$ (AR27-AR10b) we explore the effect of variable melt injection rate and duration of magmatic activity (t_f [Myr], Table 4). These experiments use a variable number of sills between 4 and 150 and a fixed time interval of either 3000 or 5000 years between two consecutive batches. The number of prescribed magma batches is chosen to represent a range of different growth histories characterized by either episodic or near continuous supply of magma (Annen 2009, 2011). Using this configuration, all the model runs in this second set have a constant time-averaged melt injection frequency of either 1.05×10^{-11} s $^{-1}$ ('high' frequency experiments) or 6.33×10^{-12} s $^{-1}$ ('low' frequency experiments) and variable duration of the magmatic activity ranging from a few thousand years to about 0.5 Myr (Table 4). The last set of experiments use a fixed number of magmatic pulses $N=25$ and variable time interval between

each pulse ranging from 250 to 31,000 years (experiments AR50-AR60, Table 4). This results into variable melt injection frequency between 1.26×10^{-10} and 1.02×10^{-12} s $^{-1}$, and variable melt injection rate between 3.58×10^{-5} and 2.89×10^{-7} m 2 s $^{-1}$. The duration of magmatic activity for this last set of experiments ranges from 6000 years to >0.7 Myr (Table 4).

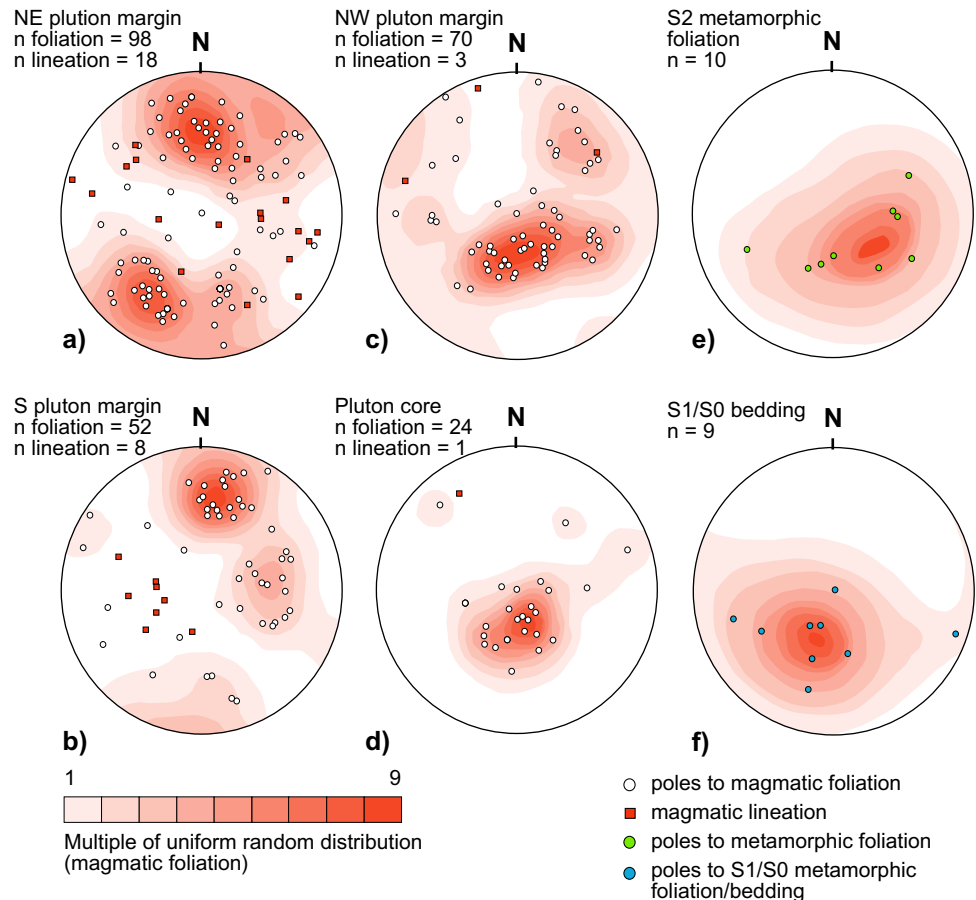
All the experiments result into three distinct groups of emplacement histories characterized by different duration of the magmatic activity mimicking fast and ultra-fast (experiments AR27/AR09 $t_f < 0.1$ Myr) to slow (experiments AR8-AR10b $t_f < 0.5$ Myr) and ultra-slow (experiment AR58, AR60 $t_p > 0.5$ Myr) evolution, covering the full spectrum of geologically meaningful accretion rates from about 5.9×10^{-9} to 9.5×10^{-11} m/s (Annen et al. 2006; Annen 2011; Caricchi et al. 2012) (Table 4).

Results

Field structural data

In the northern sector, the contact between the Arbus pluton and the metamorphic basement is flat or gently dipping,

Fig. 5 Stereonets diagrams for granodioritic rocks from Arbus pluton. **a–d** Poles to magmatic flow foliation and magmatic lineation. **e** Poles to planar cleavage S2. **f** Poles to bedding planes. All diagrams are equal area projection, lower hemisphere. For major explanation, see text



as indicated by the roughly constant elevation of the contact itself, and by the general trend of magmatic foliation (Figs. 1c, 2a, 5a, c). Here, granodiorites GD1–GD3 and the monzo-gabbronorites are generally fine- to medium-grained and develop a narrow (20–70 m) contact metamorphic aureole (Fig. 1c). Conversely, the southern margin is steeper, the magmatic foliation is locally close to vertical (Fig. 5b), and the pluton develops quite a thicker contact metamorphic aureole (600–1000 m). Metamorphic xenoliths and mafic enclaves are relatively common within a few meters of the contact with the metamorphic basement, both in the northern and southern domains (Fig. 2b, c). Size and frequency of dark enclaves generally decrease in the more felsic terms such as GD3 granodiorites and leucogranites (Fig. 2d).

The orientation of magmatic flow foliation is variable within the pluton, though the different magma batches identified on the basis of their mineralogical composition, grain size and overprinting relationships are mostly concordant (Fig. 1c). In the northern part of the pluton, the magmatic foliation is roughly parallel to the contact itself, being flat or gently dipping topside down (Fig. 1c). The magmatic lineation is extremely variable and poorly defined (Fig. 5a, c). In the southern domain, the magmatic flow foliation is steeply dipping toward the south and shows a mean EW trend parallel to the margin of the pluton (Figs. 5b, 2e). Here, a few outcrops characterized by clusters of large microgranular mafic enclaves indicate a steep magmatic lineation (Fig. 5b). The country rocks, namely the sub-greenschist facies rocks of the Arburese Unit exposed along the northern margin of the pluton and the sedimentary sequences of the Foreland show a consistent deformation fabric which includes a pervasive S1 foliation parallel to the bedding (S0, Fig. 5f). This fabric is axial planar of tight to isoclinal S-verging folds (Funedda 2009). The S1/S0 fabric is folded by a second generation of W-verging asymmetric open folds related to an axial planar cleavage S2 (Fig. 5e). Syn-magmatic deformation structures can be occasionally observed in the greenschist-facies rocks and within the inner part of the contact metamorphic aureole. They post-date the S1/S2 metamorphic fabric forming narrow, 0.1–2 m-thick, fractures parallel to the pluton

borders, frequently injected by Ti–Co–Zn–Pb ore-bearing quartzitic dykes (Fig. 2f; Moroni et al. 2019).

Microstructures

Most samples collected within the leucogranitic core of the pluton and in the innermost part of the granodioritic rim show little or no evidence for crystal-plastic deformation, as testified by the idiomorphic to sub-idiomorphic shape of late-crystallizing phases such as tourmaline (Fig. 3a), and by graphic texture of quartz-feldspar aggregates (Fig. 3b). In the relatively more mafic granodiorites of the central part of the pluton (GD3), the mafic minerals such as biotite and amphibole or pyroxene are generally idiomorphic to sub-idiomorphic and do not show sub-grains or kink folds (Fig. 3c). Plagioclase is mostly sub-idiomorphic and shows rare stress twins and oscillatory compositional zonation (Fig. 3d). K-feldspar is perthitic and frequently characterized by Carlsbad twinning (Fig. 3e). The only evidence suggestive of HT deformation ($T > 846$ K; Krhul 1996) is provided by diffuse chessboard pattern shown by interstitial quartz pockets (Fig. 3c, f). On the other hand, the relatively more mafic hornblende/pyroxene-bearing granodiorites exposed in the outermost rim of the pluton (GD1/GD2) show occasional evidence for moderate HT-deformation such as sub-grains developed at plagioclase-plagioclase contacts (Fig. 3g), tiling and syn-magmatic fracturing of plagioclase crystals (Fig. 3h).

Magnetic fabric

Table 2 gives the bulk magnitude (K_m , expressed in 10^{-5} SI) of the magnetic susceptibility at each sample site in the Arbus pluton. Overall, the low magnetic susceptibility is consistent with petrographic observation indicating ilmenite as the only Ti-Fe oxide in the rock. With few exceptions (MG), the bulk susceptibility is always below 35×10^{-5} SI (Table 2; Fig. 6a, b) in most of the samples, in agreement with the observed modal abundances of paramagnetic or diamagnetic minerals such as dark mica and quartz,

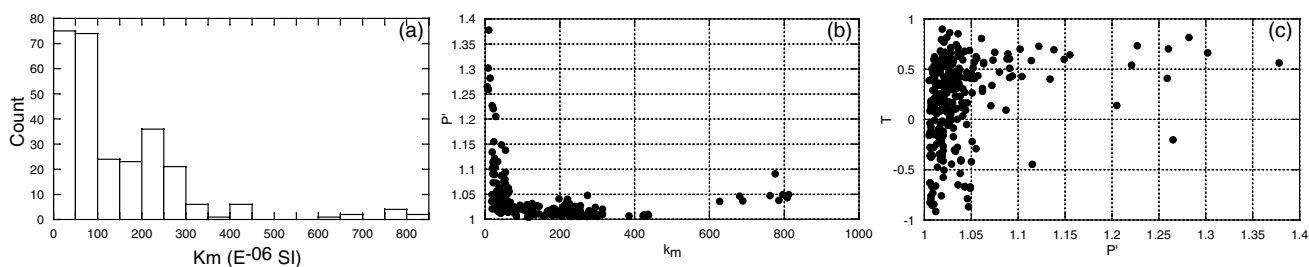


Fig. 6 Magnetic parameters for analyzed samples from Arbus pluton. **a** Distribution of bulk susceptibility (K_m). **b** Comparison between degree of anisotropy (P') and bulk susceptibility (K_m). **c** degree of anisotropy (P') and shape (T) relationships

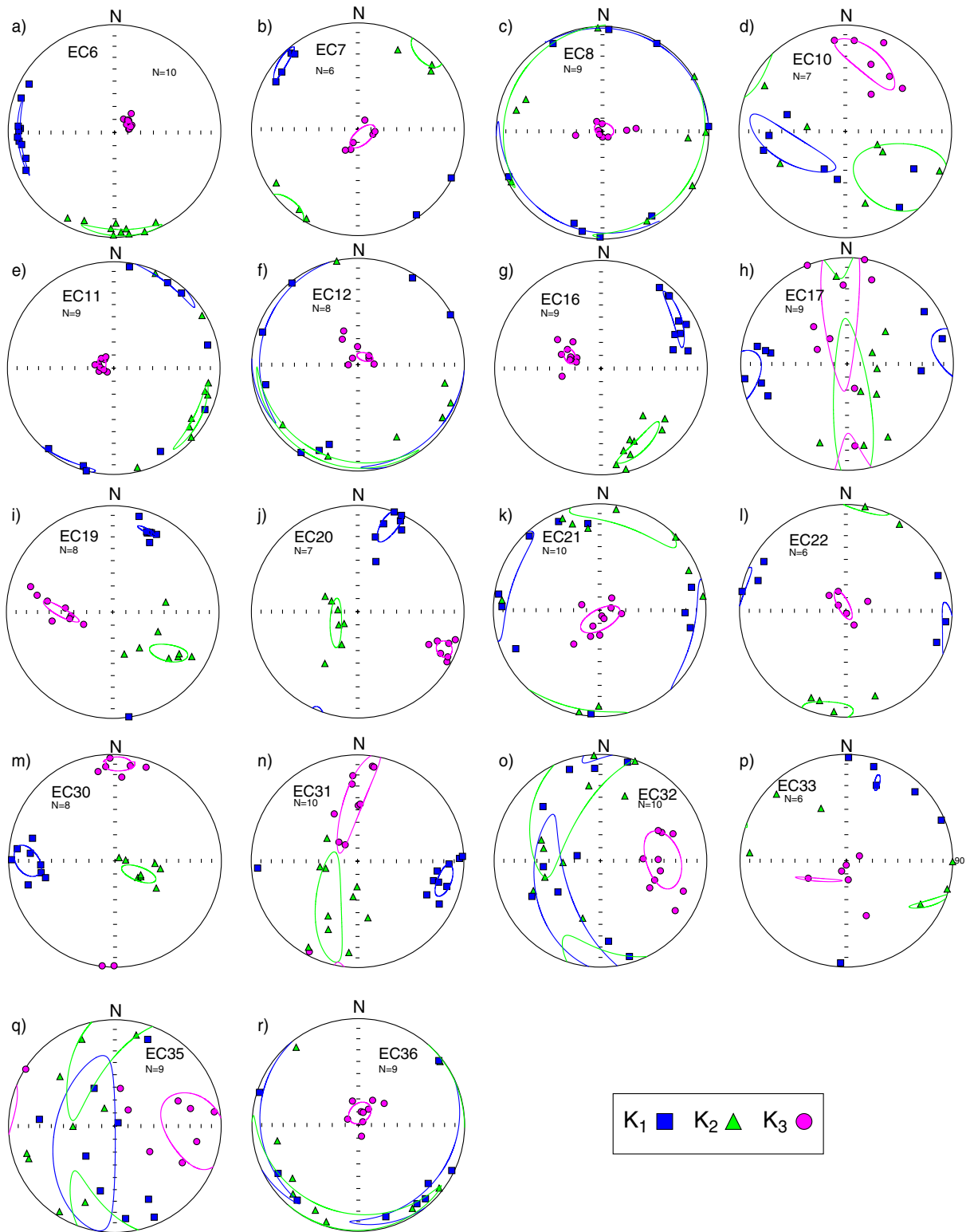
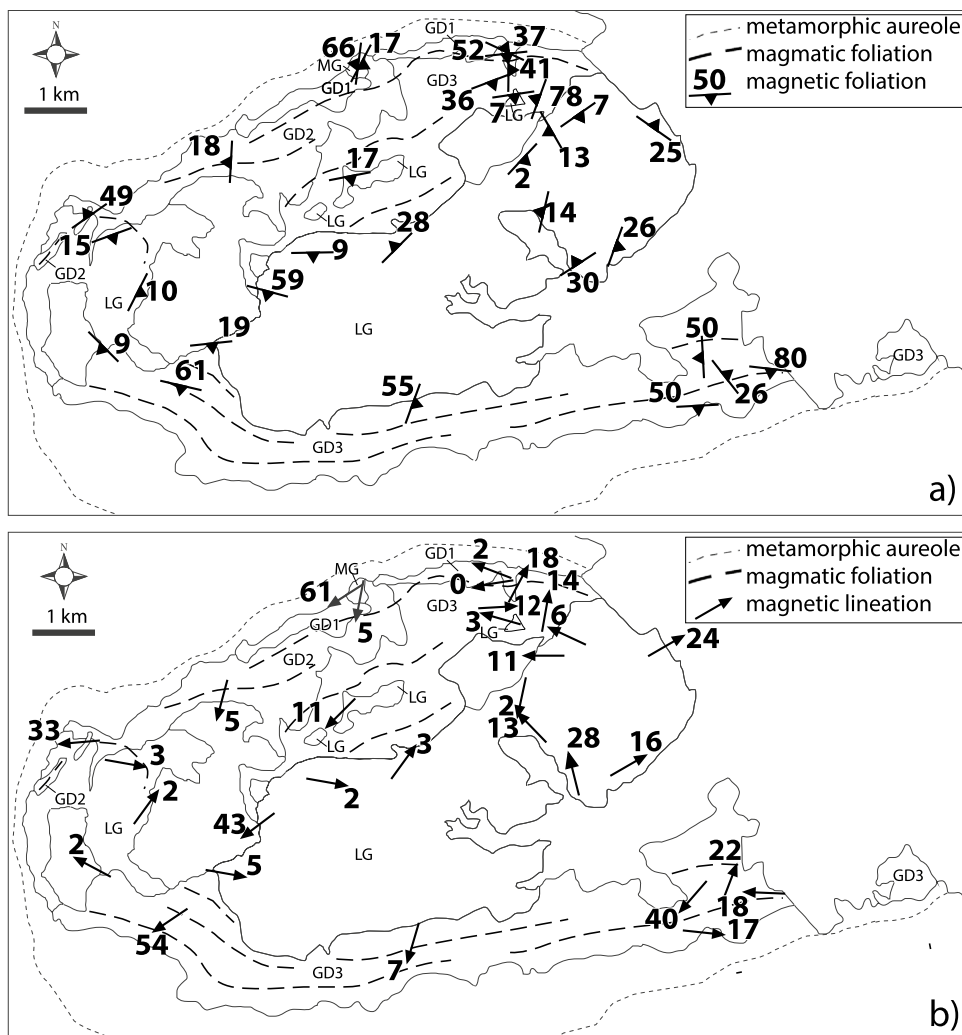


Fig. 7 Representative AMS plots from the Arbus pluton. Data are plotted on lower hemisphere, equal-area projections, in geographic coordinates. Squares, triangles, and circles represent maximum, inter-

mediate and minimum axis of magnetic susceptibility, respectively. *N* refers to number of analyzed specimens for each site

Fig. 8 Magnetic foliation (a) and lineation (b) for each sampled sites (sites names are reported in Fig. 1c)



respectively. In detail, the bulk magnetic susceptibility decreases systematically in the more evolved rocks, from 32×10^{-5} SI (pyroxene-bearing granodiorite) to 1×10^{-5} SI (hornblende-bearing leuco-granodiorite), matching the observed decrease of mafic minerals (Fig. 6a). Leucogranites show slightly higher values ($9 \pm 3 \times 10^{-5}$ SI), consistent with the modal abundance and composition of biotite (Bosi et al. 2019). The degree of anisotropy (P) is commonly low and shows average values in the range of $1.006 < P < 1.032$ (Table 2), reaching higher values of 1.38 in site EC12 (Fig. 6b, c). The magnetic fabric is generally consistent with that captured by macroscopic flow markers, although the magnetic foliation is generally better developed than magnetic lineation in most of the sites, with some exceptions (Table 2). Overall, the magnetic lineation has a generally consistent EW trend, but local deviations can be observed in the inner part of the pluton (LG, Figs. 7, 8) and along the contacts with the metamorphic basement. The magnetic foliation is more variable, though generally consistent with the macroscopic fabric recorded by micro-granular mafic

enclaves and metamorphic xenoliths (Cuccuru et al. 2016). Along the northern side of the pluton, the magnetic foliation is gently dipping to the north and roughly parallel to the border of the pluton (Figs. 7, 8). Conversely, in the southern margin the magnetic foliation is steeper (up to 80°) toward the south and southwest. The felsic core of the pluton is characterized by a NE-SW trending magnetic foliation which dips moderately to the NW or SE, defining a mostly flat sill.

Thermal models

The contact metamorphic aureole is characterized detecting the distance of the more external marker reaching a temperature of 600 K along the southern and northern margin of the pluton (W_S and W_N , respectively, Table 4). Moreover, we extrapolated also the maximum temperature recorded within 10 m from each of the pluton borders (T_S and T_N , respectively, Table 4). The first set of parametric experiments using different geothermal profiles shows that the thickness and maximum temperature of the metamorphic aureole along

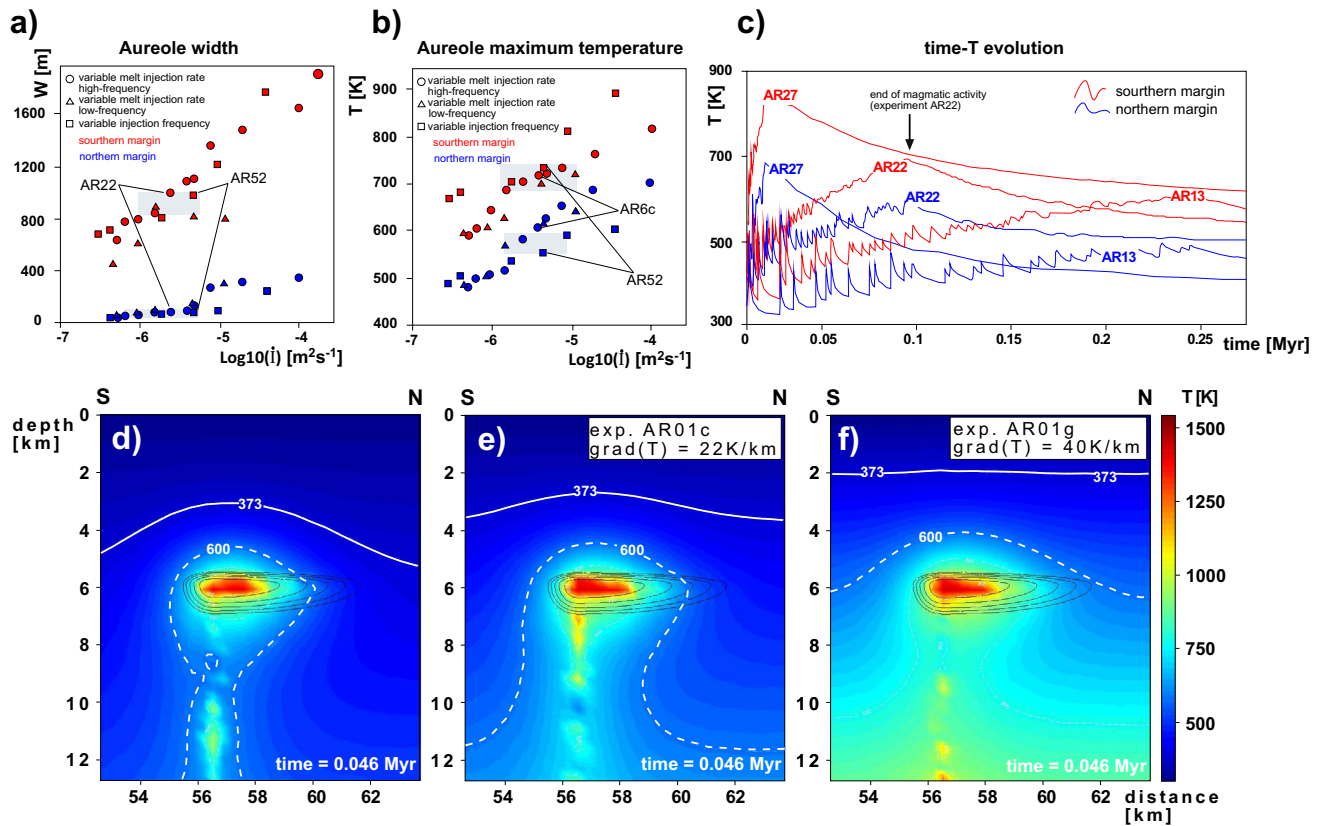


Fig. 9 Results of thermal modelling, dots and triangles denote the second set of experiments using variable melt injection rate for ‘high’ (dots) and ‘low’ frequency of injections (triangles); squares denote the third set of experiments using different injection frequencies. **a** Width of contact metamorphic aureole along the southern (red symbols) and northern (blue symbols) margins of the pluton as a function of variable melt injection rates, the gray-shaded areas indicate the range of observed width of metamorphic aureole for the admissible

melt injection rates; **b** maximum temperature recorded by the contact metamorphic aureole, same symbols as panel (a), **c** temperature evolution of the best-fit experiment (AR22) and other two selected runs using very high melt injection rate (exp. AR27) and a large number of magmatic pulses (exp. AR13); **d–f** snapshots of three representative experiments for variable initial geothermal gradients of 12, 22 and 40 K/km; the white solid line and the white dashed line indicate the trace of 373 and 600 K isotherms, respectively

the southern margin of the pluton approaches geologically realistic values of about 800–1000 m and 690–750 K for the southern margin, and < 100 m and 550–600 K for the northern margin respectively, for intermediate temperature gradients between 18 and 22 K km⁻¹ (Table 4; Fig. 9d–f). Remarkably, both too cold (12, 15 K km⁻¹) and very hot (40 K km⁻¹) initial geothermal gradients yield to thinner or thicker metamorphic aureoles and correspondingly shorter or longer cooling rates (Table 4). The second group of experiments allow to evaluate the effect of variable pluton growth rates in response to changing the number of magmatic pulses between 4 and 150 (AR27–AR10b, Table 4; Fig. 9). All these experiments use the same linear-sectioned geotherm of 20 K Km⁻¹ and two melt-injection frequencies of either $1.05 \times 10^{-11} \text{ s}^{-1}$ or $6.33 \times 10^{-12} \text{ s}^{-1}$ simulating rapidly recharging or sluggish systems, respectively. Thus, the vertical pluton growth rate change from about $2.37 \times 10^{-9} \text{ ms}^{-1}$ using 4 pulses (experiment AR24, Table 4) to $9.5 \times 10^{-11} \text{ ms}^{-1}$ using 100 pulses (experiment AR10b

100, Table 4, Fig. 9). The extension of metamorphic aureoles generally depends on the emplacement temperature of magma and the time required to cool it (Annen et al. 2006; Annen 2017). Thus, at low P,T conditions such as those inferred for the Arbus pluton, the thickness of the metamorphic aureole is positively correlated with the pluton growth rate as efficient dissipation by the country rocks is expected to prevent heat diffusion over large distances. Yet, the experiments with few magmatic pulses and high pluton growth rates above $2 \times 10^{-9} \text{ ms}^{-1}$ (experiments AR27, AR04, Table 4; Fig. 9c) develop too hot and unrealistically thick metamorphic aureole that does not match the field data. This discrepancy is particularly obvious along the northern side of the pluton where model runs predict >300 m-wide aureole but the observed thickness is generally less than 100 m (Table 4). Moreover, these experiments are characterized by very short lifetime of the magmatic system, generally below 0.03 Myr corresponding to nearly instantaneous emplacement (Table 4; Fig. 9). Conversely, the experiments with a

relatively large number of magmatic pulses between about 16–32 reproduce quite well the observed thickness of the metamorphic aureole (experiments AR05, AR6c and AR22; Table 4; Fig. 9a). The last group of experiments assume a constant number of magmatic pulses $N=25$, thus the pluton growth rate changes as a function of variable melt-injection frequency (AR50–AR60, Table 4). These experiments reproduce reasonably the temperatures recorded along both pluton's margins (Fig. 9b), though the thickness of the metamorphic aureole is reproduced only for intermediate to low melt injection frequencies between about 1.5×10^{-11} and $6.3 \times 10^{-12} \text{ s}^{-1}$ yielding to pluton growth rates between 1.8×10^{-6} and $4.5 \times 10^{-6} \text{ ms}^{-1}$ (AR52–AR53, Fig. 9).

Discussion

Time-integrated emplacement history

The relatively low temperature recorded by the country rocks in the immediate proximity of the pluton ($T < 740 \text{ K}$; Secchi et al. 1991; Bosi et al. 2018) and the internal contacts between compositionally different magma batches indicates that accretion of Arbus pluton was incremental, rather than resulting from a single injection episode (Cuccuru et al. 2016). The strongly asymmetric contact metamorphic aureole suggests that magma increments were not injected in the central part of the pluton, but probably close to its southern margin where the aureole reaches its maximum thickness. According to Cuccuru et al. (2016), the injection of magma follows an EW shear zone reactivating the Arburese Frontal Thrust (Fig. 1b). The combination of AMS analysis and thermal modelling allow to refine the proposed emplacement model. The mostly flat magmatic and magnetic fabric observed in the northern margin and central part of the pluton indicates that these domains represent the roof-wall transition zone and the remnant of the pluton roof, respectively. The horizontal compositional layering suggests that construction of the uppermost part of the magmatic chamber involved repeated injections of relatively thin sill-shaped dykes. On the contrary, the southern half of Arbus pluton, characterized by a steep magmatic and magnetic fabric, nearly absence of stoped blocks and generally more mafic composition consisting of a thick layer of hornblende-bearing granodiorite, likely represents the pluton floor/feeder dyke transition zone (Fig. 1). According to this interpretation, the small gabbro-norite body and the thin discontinuous layer of pyroxene-bearing granodiorite exposed along the northern margin of the pluton represent a remnant of the feeder zone separated from the southern border by subsequent emplacement of more differentiated magma batches in the core of the pluton. The relatively scattered orientation of the magmatic fabric and the minimal

syn-magmatic deformation of the host rocks in the central and northern part of the pluton indicate that magma injection involved passive reactivation of the Arburese Frontal Thrust (Funedda 2009) which served as permeable horizon facilitating the lateral spreading of magma. Independent constraints provided by clustered U–Pb zircon ages and thermal modelling indicate that cooling of the pluton required probably less than 0.3–0.5 Myr. This observation implies that the contribution of dilatant deformation would be negligible in the range of geologically meaningful strain rates between 1×10^{-12} to $1 \times 10^{-15} \text{ s}^{-1}$ (Turcotte and Schubert 2002). Therefore, accretion of the pluton roof is much likely controlled by structural inheritance, rather than regional tectonics. Yet, the country rocks preserves evidence for syn-magmatic deformation. The SW border of the pluton, in fact, record sub-solidus strain compatible with syn-tectonic injection of mafic to intermediate melts within the Arbus-Capo Pecora Shear Zone (Fig. 1), a major top-to-the W structure belonging to the regional network of Late Variscan shear zones (i.e., Matte 2001; Casini et al. 2012, 2015a, b; Casini and Funedda 2014; Musumeci et al. 2015). Overall, these observations fit well a model of incremental emplacement of multiple dykes forming an asymmetric laccolith with the vertical feeder zone localized in the southern half of the pluton (Fig. 9), representing a sort of infra-crustal magmatic channel connecting a not exposed source zone to the upper-crustal magma chamber (Cruden et al. 1999). The orientation of this vertical channel percolated by melt coincides with the orientation of Capo Pecora Shear Zone (Fig. 1b), thus we propose that melt ascent pathway is mostly controlled by dynamic pressure established within the shear zone during viscous deformation (i.e., Luisier et al. 2019).

Although all models simulate repeated injections of magma localizing the vertical feeder zone in the southern half of the pluton, several first-order outcomes such as thickness and maximum temperature of the metamorphic aureole, and the cooling time of the magmatic system change as a function of the emplacement rate and the frequency of injections (Table 4; Fig. 9c). The models providing a better fit to geological and geochronological constraints have been obtained combining a moderate to large number of magmatic pulses, roughly between 20 and 50, low melt injection rates in the range of $3\text{--}8 \times 10^{-10} \text{ ms}^{-1}$ and moderately high frequency of injections between 1 and $1.5 \times 10^{-11} \text{ s}^{-1}$ (Table 4; Fig. 9). In particular, the experiments AR6c and AR22 develop a strongly asymmetric metamorphic aureole which is up to 850–1100 m-thick in the southern margin and less than 100 m to the north (Table 4; Fig. 9a). Another relevant feature of these experiments is the development of peak metamorphic temperatures consistent with geological observation (Secchi et al. 1991; Bosi et al. 2018). The southern margin, in fact, records temperature exceeding 700–730 K, whereas the northern contact is characterized by temperature

between about 550 and 600 K (Fig. 9b; Table 4). It should be emphasized that the formulation of the heat equation (Eq. 1) explicitly neglects the contribution of shear and adiabatic heating. However, the contribution of these thermal sources should be very small at upper crustal conditions such as those deduced for emplacement of the Arbus pluton, because of small pressure changes and low inelastic viscous deformation (i.e., Burg and Gerya 2005).

Implications for late Variscan geodynamics

The emplacement of granitoids in orogenic settings is often, if not systematically, correlated to activation of major shear zones which provide efficient melt pathways (Rosenberg and Handy 2005; Vilà et al. 2010). The growth of Arbus pluton confirms this paradigm, as near-vertical magmatic flow trajectories combined with horizontal stretching lineation call for emplacement within an EW strike-slip shear zone (Cuccuru et al. 2016). Yet, AMS investigation combined with field structural analysis and thermal modelling evidenced a more complex tectonic setting. The central and northern sectors, in fact, reflect mostly horizontal magma flow and weak or absent sub-magmatic deformation, which is not consistent with a model of syntectonic emplacement

during shear. These observations suggest that accretion of the pluton likely involved transtensional reactivation of the Arburese Frontal Thrust (Fig. 1) which served as permeable horizon facilitating the switch from vertical flow to lateral expansion above the pluton floor (Fig. 10). The causal relationships linking the Arbus pluton to the general geodynamic framework are not straightforward, as lithospheric-scale shearing is widespread in the Variscan belt during the Carboniferous-Permian transition (Matte 2001; Carosi et al. 2012; Oggiano et al. 2009; Casini and Funedda 2014; Edel et al. 2014; Casini et al. 2015a). Palaeomagnetic data, field structural evidence and U–Pb zircon dating indicate that in Sardinia shearing was mostly coeval with a 90° clockwise rotation of the Corsica-Sardinia-Maures-Esterel block, accompanied by a large, >1000 km, horizontal displacement along a lithospheric-scale right-lateral shear zone (Muttoni et al. 2003; Edel et al. 2014). The rotation was accommodated in the interior of the block by development of both left- and right-lateral strike-slip shear zones, frequently injected by syntectonic melts of various composition dated between 305 and 295 Ma (e.g., Casini et al. 2012; Casini et al. 2015a; Musumeci et al. 2015; Meloni et al. 2017). The emplacement of Arbus pluton might be recast into this general geodynamic framework by complementing the results obtained in this study with the existent field structural data and geochronological constraints on two adjacent Carboniferous-Permian intrusive massifs. The first, namely the Mandrolisai pluton (Fig. 11) is almost made-up of hornblende biotite to biotite granodioritic magmas emplaced at about 299 Ma reactivating an early Carboniferous structure equivalent of the Arburese Frontal Thrust (Meloni et al. 2017). The second, (Monte Grighini pluton) is conversely a peraluminous, strongly deformed syntectonic granodiorite, emplaced between 300 and 302 Ma within a segment of a stair-stepped NW trending dextral shear zone (Musumeci et al. 2015). Remarkably, restoring the pre-rotational position of the Corsica-Sardinia block (Edel et al. 2014), the direction of this shear zone (Central Sardinia Shear Zone, Fig. 11) is perfectly coincident with that of the Bray fault zone, which is one of the main Late Variscan structures responsible for accommodating the large rotation of crustal blocks during self-subduction of Pangea and opening of Tethys at the end of the Variscan orogeny (Muttoni et al. 2003; Gutiérrez-Alonso et al. 2009). Although the correlation between the Bray Fault zone and the Central Sardinia Shear Zone is only speculative, we must emphasize that structures with similar orientation and equivalent kinematic are widespread all over the Variscan chain (Matte 2001; Edel et al. 2014; Rossi et al. 2015). Thus, the various segments of the Central Sardinia Shear Zone likely reflect upper crustal strain partitioning of a major lithospheric-scale structure which might have enhanced the ascent of melt from the lower crust and the mantle-crust interface (Rossi et al. 2015; Conte et al.

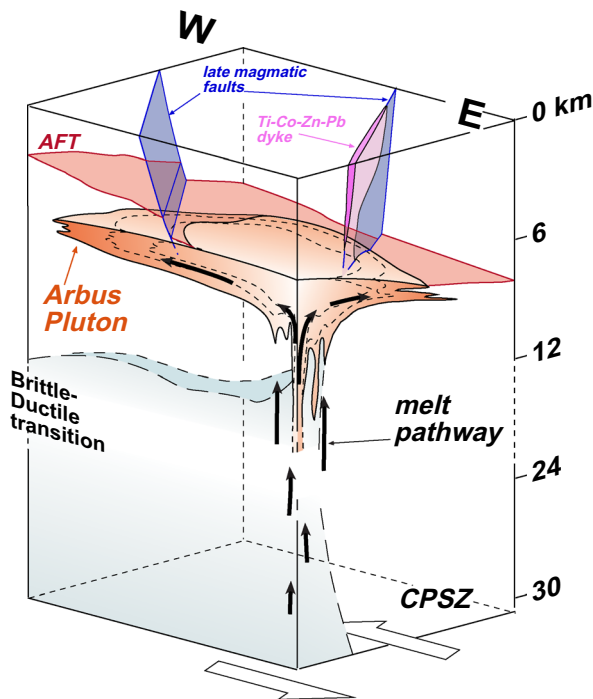


Fig. 10 Conceptual model of emplacement of Arbus Pluton (not to scale). The pluton builds up by incremental emplacement of several magma batches injecting through the Capo Pecora Shear Zone (CPSZ). The Arburese Frontal Thrust (AFT) acts as a mechanical discontinuity facilitating the switch from vertical to horizontal magma flow

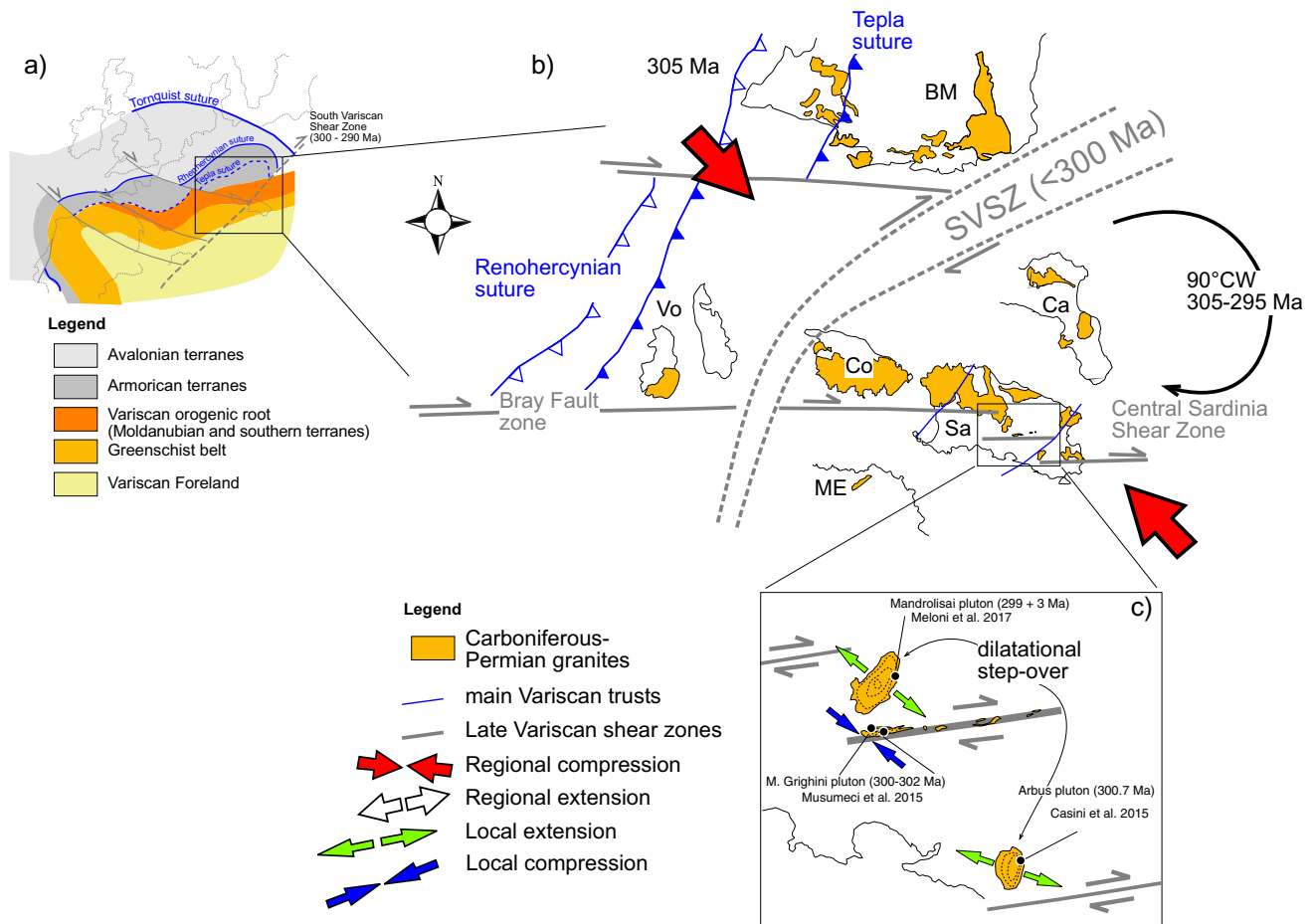


Fig. 11 Synthetic structural model for the Carboniferous-Permian magmatism of Sardinia in relation with the phase of late-Variscan shearing. The principal late-Variscan structures are indicated, alto-

gether with the boundaries of the main Variscan domains in their inferred pre-Permian position (Edel et al. 2014). BM=Bohemian Massif, Co=Corsica, Sa=Sardinia, Ca=Calabria

2017). Therefore, we propose that Arbus and Mandrolisai plutons emplaced at dilatational step-overs recording poor deformation, whereas the Monte Grighini pluton injected a locally compressive segment of the shear zone. Therefore, according to this simple model, the observed differences in composition, volume of magma and deformation intensity of the three plutons simply reflect the local re-orientation of the stress field along the shear zone.

Conclusions

AMS data and field structural observation confirm the general architecture of the Arbus Pluton depicted in Cuccuru et al. (2016). Based on these structural arguments and the results obtained from a suite of 2D thermal experiments, we propose an emplacement model by fault-assisted magma injection within a dilatational site developed along a regional strike-slip shear zone (Cruden et al. 1999; Tikoff and Teysier 1992; Yoshinobu et al. 1998). According to this model,

the growth of the pluton likely required relatively low emplacement rates combined with high fault displacement rate (Yoshinobu et al. 1998). The geometry of the pluton roof and that of the roof-wall transition zone depart from this simple fault-assisted model, as melt flow above the feeder zone was apparently controlled by structural inheritance rather than active deformation, thus resulting into an abrupt switch from sin-magmatic shear to stoping and horizontal expansion. The proposed emplacement model fits the general framework of Late Variscan geodynamics connected to the rotation of crustal blocks during trans-lithospheric shearing related to self-subduction of Pangea.

Acknowledgements This work was supported by Fondo di Ateneo per la Ricerca FAR2020 (Università di Sassari, Sassari, Italy) and by RAS L.R. 7/2007 research program 'Il blocco Sardo-Corso: area chiave per la ricostruzione della geodinamica Variscica' CUP J81G17000110002. The Grant to Department of Science, Roma Tre University (MIUR-Italy Dipartimenti di Eccellenza, ARTICOLO 1, COMMI 314 – 337 LEGGE 232/2016) is also gratefully acknowledged.

Open Access This article is licensed under a Creative Commons Attribution 4.0 International License, which permits use, sharing, adaptation, distribution and reproduction in any medium or format, as long as you give appropriate credit to the original author(s) and the source, provide a link to the Creative Commons licence, and indicate if changes were made. The images or other third party material in this article are included in the article's Creative Commons licence, unless indicated otherwise in a credit line to the material. If material is not included in the article's Creative Commons licence and your intended use is not permitted by statutory regulation or exceeds the permitted use, you will need to obtain permission directly from the copyright holder. To view a copy of this licence, visit <http://creativecommons.org/licenses/by/4.0/>.

References

- Albert H, Larrea P, Costa F, Widom E, Siebe C (2020) Crystals reveal magma convection and melt transport in dyke-fed eruptions. *Sci Rep* 10:11632. <https://doi.org/10.1038/s41598-020-68421-4>
- Annen C (2009) From plutons to magma chambers: Thermal constraints on the accumulation of eruptible silicic magma in the upper crust. *Earth Planet Sci Lett* 284:409–416
- Annen C (2011) Implications of incremental emplacement of magma bodies for magma differentiation, thermal aureole dimensions and plutonism volcanism relationships. *Tectonophysics* 500:3–10. <https://doi.org/10.1016/j.tecto.2009.04.010>
- Annen C (2017) Factors affecting the thickness of metamorphic aureole. *Front Earth Sci*. <https://doi.org/10.3389/feart.2017.00082>
- Annen C, Scaillet B, Sparks RSJ (2006) Thermal constraints on the emplacement rate of a large intrusive complex: the Manaslu Leucogranite, Nepal Himalaya. *J Petrol* 47:71–95. <https://doi.org/10.1093/petrology/egi068>
- Aranguren A, Cuevas J, Tubía JM, Román-Berdiel T, Casas-Sainz A, Casas-Ponsati A (2003) Granite laccolith emplacement in the Iberian arc: AMS and gravity study of the La Tojiza pluton (NW Sapin). *J Geol Soc Lond* 160:435–445
- Barboni M, Schoene B (2014) Short eruption window revealed by absolute crystal growth rates in a granitic magma. *Nat Geosci* 7:525–528
- Boni M, Stein HJ, Zimmerman A, Villa IM (2003) Re-Os age for molybdenite from SW Sardinia (Italy): a comparison with $^{40}\text{Ar}/^{39}\text{Ar}$ dating of Variscan granitoids. In: Eliopoulos DG (Ed.), *Mineral exploration and sustainable development. Proceedings 7th Biennial SGA Meeting*, Athens, Greece. Volume 1. Millpress, Rotterdam, 247–250
- Bosi F, Naitza S, Skogby H, Secchi F, Conte AM, Cuccuru S, Hålenius U, De La Rosa N, Kristiansson P, Charlotta Nilsson EJ, Ros L, Andreozzi GB (2018) Late magmatic controls on the origin of schorlitic and foititic tourmalines from late-Variscan peraluminous granites of the Arbus igneous complex (SW Sardinia, Italy): crystal-chemical study and petrological constraints. *Lithos* 308–309:395–411
- Bosi F, Naitza S, Secchi F, Conte AM, Cuccuru S, Andreozzi GB, Skogby H, Hålenius U (2019) Petrogenetic controls on the origin of tourmalinite veins from Mandrolisai igneous massif (central Sardinia, Italy): insights from tourmaline crystal chemistry. *Lithos* 342–343:333–344
- Bouchez JL (1997) *Granite is never isotropic: an introduction to AMS studies of granitic rocks*. Kluwer Academic Publishers, Alphen aan den Rijn, pp 95–112
- Bouchez JL, Gleizes G, Djouadi T, Rochette P (1990) Microstructure and magnetic susceptibility applied to emplacement kinematics of granites: the example of the Foix pluton (French Pyrenees). *Tectonophysics* 184:157–171
- Brown M (2013) Granite: From genesis to emplacement. *Geol Soc Am Bull* 125(7–8):1079–1113
- Burg JP, Gerya T (2005) The role of viscous heating in Barrovian metamorphism of collisional orogens: thermomechanical models and application to the Lepontine Dome in the Central Alps. *J Metamorph Geol* 23:75–95. <https://doi.org/10.1111/j.1525-1314.2005.00563.x>
- Caricchi L, Annen C, Rust A, Blundy J (2012) Insights into the mechanisms and timescales of pluton assembly from deformation patterns of mafic enclaves. *J Geophys Res* 117(B11206):1–18
- Carosi R, Montomoli C, Tiepolo M, Frassi C (2012) Geochronological constraints on post-collisional shear zones in the Variscides of Sardinia (Italy). *Terra Nova* 24:42–51
- Casini L (2012) A Matlab-derived software(geothermMOD1.2) for one-dimensional thermal modeling, and its application to the Corsica-Sardinia batholith. *Comput Geosc* 45:82–86. <https://doi.org/10.1016/j.cageo.2011.10.020>
- Casini L, Funedda A (2014) Potential of pressure solution for strain localization in the Baccu Locci Shear Zone (Sardinia, Italy). *J Struct Geol* 66:188–204. <https://doi.org/10.1016/j.jsg.2014.05.016>
- Casini L, Maino M (2018) 2D-thermo-mechanical modelling of spatial *P-T* variations in heterogeneous shear zones. *Italian J Geosci* 137:272–282. <https://doi.org/10.3301/IJG.2018.13>
- Casini L, Funedda A, Oggiano G (2010) A balanced foreland–hinterland deformation model for the Southern Variscan belt of Sardinia, Italy. *Geol J* 45:634–649
- Casini L, Cuccuru S, Maino M, Oggiano G, Tiepolo M (2012) Emplacement of the Arzachena pluton (Corsica-Sardinia batholith) and the geodynamics of the incoming Pangea. *Tectonophysics* 544–545:31–49
- Casini L, Puccini A, Cuccuru S, Maino M, Oggiano G (2013) – GEO-THERM: A finite-difference code for testing metamorphic *P-T-t* paths and tectonic models. *Comput Geosci* 59:171–180
- Casini L, Cuccuru S, Puccini A, Oggiano G, Rossi Ph (2015a) Evolution of the Corsica-Sardinia batholith and late-orogenic shearing of the Variscides. *Tectonophysics* 646:65–78
- Casini L, Cuccuru S, Maino M, Oggiano G, Puccini A, Rossi Ph (2015b) Structural map of Variscan northern Sardinia (Italy). *J Maps* 11:75–84. <https://doi.org/10.1080/17445647.2014.936914>
- Cifelli F, Minelli L, Rossetti F, Mattei M (2012) The emplacement of the Late Miocene Monte Capanne intrusion (Elba Island, Central Italy): constraint from magnetic fabric analyses. *Int J Earth Sci* 101:787–802. <https://doi.org/10.1007/s00531-011-0701-z>
- Cocherie A, Rossi P, Fanning CM, Guerrot C (2005) Comparative use of TIMS and SHRIMP for U-Pb zircon dating of A-type granites and mafic tholeiitic layered complexes and dykes from the Corsican Batholith (France). *Lithos* 82:185–219
- Cogné JP, Perroud H (1988) Anisotropy of magnetic susceptibility as a strain gauge in the Flamanville granite, NW France. *Phys Earth Planet Interiors* 51:264–270
- Conte AM, Cuccuru S, D'Antonio M, Naitza S, Oggiano G, Secchi F, Casini L, Cifelli F (2017) The post-collisional late Variscan ferroan granites of southern Sardinia (Italy): inferences for inhomogeneity of lower crust. *Lithos* 294–295:263–282
- Conti P, Carmignani L, Oggiano G, Funedda A, Eltrudis A (1998) Late orogenic collapse and the unroofing history of the Variscan basement of southern Sardinia (Italy). *Acta Univ Carol Geol* 42:222–223
- Conti P, Carmignani L, Funedda A (2001) Change of nappe transport direction during the Variscan collisional evolution of central-southern Sardinia (Italy). *Tectonophysics* 332:255–273
- Crank J, Nicholson P (1947) A practical method for numerical evaluation of partial differential equations of the heat conduction type. *Proc Camb Phil Soc* 43:50–67
- Cruden AR, Tobisch OT, Launeau P (1999) Magnetic fabric evidence for conduit-fed emplacement of a tabular intrusion: Dinkey Creek

- Pluton, central Sierra Nevada batholith, California. *J Geophys Res* 104(B5):10511–10530
- Cuccuru S, Casini L, Oggiano G, Cherchi GP (2012) Can weathering improve the toughness of a fractured rock? A case study using the San Giacomo granite. *Bull Eng Geol Environ* 71:557–567. <https://doi.org/10.1007/s10064-012-0416-9>
- Cuccuru S, Naitza S, Secchi F, Puccini A, Casini L, Pavanetto P, Linnemann U, Hofmann M, Oggiano G (2016) Structural and metallogenic map of late Variscan Arbus igneous complex (SW Sardinia, Italy). *J Maps* 12:860–865
- Edel JB, Casini L, Oggiano G, Rossi P, Schulmann K (2014) Early Permian 90° clockwise rotation of the Maures–Estérel–Corsica–Sardinia block confirmed by new palaeomagnetic data and followed by a Triassic 60° clockwise rotation. In: Schulmann K, Martínez Catalán JR, Lardeaux JM, Janoušek V, Oggiano G (eds) *The Variscan orogeny: extent, timescale and the formation of the European crust*. Geological Society, London, pp 333–361
- Ellwood BB, Whitney JA (1980) Magnetic fabric of the Elberton Granite, northeast Georgia. *J Geophys Res* 85:1481–1486
- Funedda A (2009) Foreland – and hinterland-verging structures in fold-and-thrust belt: an example from the Variscan foreland of Sardinia. *Int J Earth Sci* 98(7):1625–1642. <https://doi.org/10.1007/s00531-008-0327-y>
- Gattacceca J, Orsini JB, Bellot JP, Cherchi G (2004) Magnetic fabric of granitoids from Southern Corsica and Northern Sardinia and implications for Late Hercynian tectonic setting. *J Geol Soc Lond* 161:277–289. <https://doi.org/10.1144/0016-764903-115>
- Gébelin A, Roger F, Brunel M (2009) Syntectonic crustal melting and high-grade metamorphism in a transpressional regime, Variscan Massif Central, France. *Tectonophysics* 477(3–4):229–243. <https://doi.org/10.1016/j.tecto.2009.03.022>
- Guillet P, Bouchez JL, Wagner JJ (1983) Anisotropy of magnetic susceptibility and magmatic structures in the Guérande granite massif (France). *Tectonics* 2:419–429
- Gutiérrez-Alonso G, Fernández-Suarez J, Weil AB, Brendan Murphy J, Damian Nance R, Corfú F, Johnston ST (2008) Self-subduction of the Pangaeon global plate. *Nat Geosci* 1(8):549–553. <https://doi.org/10.1038/ngeo250>
- Heller F (1973) Magnetic anisotropy of granitic rocks of the Bergell massif (Switzerland). *Earth Planet Sci Lett* 20:180–188
- Hrouda F (1982) Magnetic anisotropy of rocks and its application in geology and geophysics. *Geoph Surv* 5:37–82
- Jelinek V (1977) The statistical theory of measuring anisotropy of magnetic susceptibility of rocks and its application. *Geofyzika Brno, Brno*, pp 1–88
- Jelinek V (1981) Characterization of the magnetic fabric of rocks. *Tectonophysics* 79:63–67
- King RF (1966) The magnetic fabric in some Irish granites. *Geol J* 5:43–66
- Kratinova Z, Schulmann K, Hrouda F, Shail R (2003) The role of regional tectonics and magma flow coupling versus magmatic processes in generating contrasting magmatic fabrics within the Land's End Granite, Cornwall. *Geosci South-West Engl* 10:442–448
- Kretz R (1983) Symbols for rock-forming minerals. *Am Min* 68:277–279
- Le Bas MJ, Streckeisen AL (1991) The IUGS systematics of igneous rocks. *J Geol Soc Lond* 148:825–833
- Luisier C, Baumgartner L, Schmalholz SM, Siron G, Vennemann T (2019) Metamorphic pressure variation in a coherent Alpine nappe challenges lithostatic pressure paradigm. *Nat Geosci* 10(1):4734
- Maino M, Casini L, Ceriani A, Decarlis A, Di Giulio A, Seno S, Setti M, Stuart FM (2015) Dating shallow thrust with zircon (U-Th) thermochronometry – the shear heating connection. *Geology* 43:495–498. <https://doi.org/10.1130/G36492.1>
- Maino M, Casini L, Boschi C, Di Giulio A, Setti M, Seno S (2020) Time-dependent heat budget of a thrust from geological records and numerical experiments. *J Geophys Res Solid Earth* 125:2019JB018940. <https://doi.org/10.1029/2019JB018940>
- Matte P (2001) The Variscan collage and orogeny (480–290 Ma) and the tectonic definition of the Armorica microplate: a review. *Terra Nova* 13:122–128. <https://doi.org/10.1046/j.1365-3121.2001.00327.x>
- Meloni MA, Oggiano G, Funedda A, Pistis M, Linnemann U (2017) Tectonics, ore bodies, and gamma-ray logging of the Variscan basement, southern Gennargentu massif (Central Sardinia, Italy). *J Maps* 13:196–206
- Moroni M, Naitza S, Ruggieri G, Aquino A, Costagliola P, De Giudici G, Caruso S, Ferrari E, Fiorentini ML, Lattanzi P (2019) The Pb–Zn–Ag vein system at Montevecchio–Ingurtosu, southwestern Sardinia, Italy: a summary of previous knowledge and new mineralogical, fluid inclusion, and isotopic data. *Ore Geol Rev* 115:103194. <https://doi.org/10.1016/j.oregeorev.2019.103194>
- Musumeci G, Spano ME, Cherchi GP, Franceschelli M, Pertusati PC, Cruciani G (2015) Geological map of the Monte Grighini Variscan Complex (Sardinia, Italy). *J Maps* 11:287–298
- Muttoni G, Kent DV, Garzanti E, Brack P, Abrahamsen N, Gaetani M (2003) Early Permian Pangaea ‘B’ to late Permian Pangaea ‘A’. *Earth Planet Sci Lett* 215:379–394
- Naitza S, Conte AM, Cuccuru S, Oggiano G, Secchi F, Tecce F (2017) A Late Variscan tin province associated to the ilmenite-series granites of the Sardinian Batholith (Italy): the Sn and Mo mineralisation around the Monte Linas ferroan granite. *Ore Geol Rev* 80:1259–1278
- Oggiano G, Funedda A, Carmignani L, Pasci S (2009) The Sardinia-Corsica microplate and its role in the Northern Apennine Geodynamics: New insights from the Tertiary intraplate strike-slip tectonics of Sardinia. *Boll Soc Geol Ital* 128(2):527–539
- Paterson SR, Ardill K, Vernon R, Žák J (2019) A review of mesoscopic magmatic structures and their potential for evaluating the hypersolidus evolution of intrusive complexes. *J Struct Geol* 125:134–147
- Puccini A, Xhixha G, Cuccuru S, Oggiano G, Xhixha MK, Mantovani F et al (2014) Radiological characterization of granitoid outcrops and dimension stones of the Variscan Corsica-Sardinia Batholith. *Environ Earth Sci* 71(1):393–405. <https://doi.org/10.1007/s12665-013-2442-8>
- Rosenberg CL, Handy MR (2005) Experimental deformation of partially melted granite revisited: implications for the continental crust. *J Metamorph Geol* 23:19–28. <https://doi.org/10.1111/j.1525-1314.2005.00555.x>
- Rossi Ph, Cocherie A, Fanning CM (2015) Evidence in Variscan Corsica of a brief and voluminous late Carboniferous to early Permian volcanic-plutonic event contemporaneous with a high-temperature/low-pressure metamorphic peak in the lower crust. *Bull Soc Géol Fr* 186:171–192
- Sant’Ovaia H, Olivier P, Ferreira N, Noronha F, Leblanc D (2010) Magmatic structures and kinematics emplacement of the Variscan granites from Central Portugal (Serra da Estrela and Castro Daire areas). *J Struct Geol* 32(10):1450–1465
- Secchi F, D’Antonio M (1996) Inferences of Sr, Nd and O isotopic tracers on the origin and evolution of a gabbro-norite-granodiorite sequence from southern Hercynian chain of Sardinia. A case study from the Arburése igneous complex and its comparison with the earlier sequences of Sàrrabus area. *Period Mineral* 65:257–273
- Secchi F, Brotzu P, Callegari E (1991) The Arburése igneous complex (SW Sardinia, Italy) – an example of dominant igneous

- fractionation leading to peraluminous cordierite-bearing leucogranites as residual melts. *Chem Geol* 92:213–249
- Tikoff B, Teyssier C (1992) Crustal-scale, en echelon P-shear tensional bridges— a possible solution to the batholithic room problem. *Geology* 20:927–930
- Van der Voo R, Klootwijk CT (1972) Paleomagnetic reconnaissance study of the Flamanville granite with a special reference to the anisotropy of its susceptibility. *Geol Mijnbouw* 51:609–617
- Vernon RH, Johnson SE, Melis EA (2004) Emplacement-related microstructures in the margin of a deformed pluton: the San José tonalite, Baja California, México. *J Struct Geol* 26(10):1867–1884
- Vilà M, Fernández M, Jiménez-Munt I (2010) Radiogenic heat production variability of some common lithological groups and its significance to lithospheric thermal modeling. *Tectonophysics* 490:152–164. <https://doi.org/10.1016/j.tecto.2010.05.003>
- Vosteen H-D, Schellschmidt R (2003) Influence of temperature on thermal conductivity, thermal capacity and thermal diffusivity for different types of rock. *Phys Chem Earth a/b/c* 28:499–509
- Wei CJ, Powell R, Clarke G (2004) Calculated phase equilibria for low- and medium-pressure metapelites in the KFMASH and KMnF-MASH systems. *J Metamorph Geol* 22:495–508
- Whitney DL, Evans BW (2010) Abbreviations for names of rock-forming minerals. *Am Mineral* 95:185–187
- Whittington AG, Hofmeister AM, Nabelek PI (2009) Temperature-dependent thermal diffusivity of the Earth's crust and implications for magmatism. *Nature* 458:319–321
- Yang XM (2017) Estimation of crystallization pressure of granite intrusions. *Lithos* 286–287(2017):324–329
- Yoshinobu AS, Okaya DA, Paterson SR (1998) Modeling the thermal evolution of fault-controlled magma emplacement models: implications for the solidification of granitoid plutons. *J Struct Geol* 20:1205–1218. [https://doi.org/10.1016/S0191-8141\(98\)00064-9](https://doi.org/10.1016/S0191-8141(98)00064-9)